FINITE ELEMENT ANALYSIS OF THREE-PHASE PIEZOELECTRIC NANOCOMPOSITES

A Thesis

by

KEVIN S. MAXWELL

Submitted to the Office of Graduate Studies of
Texas A&M University
in partial fulfillment of the requirements for the degree of

MASTER OF SCIENCE

August 2009

Major Subject: Aerospace Engineering

FINITE ELEMENT ANALYSIS OF THREE-PHASE PIEZOELECTRIC NANOCOMPOSITES

A Thesis

by

KEVIN S. MAXWELL

Submitted to the Office of Graduate Studies of
Texas A&M University
in partial fulfillment of the requirements for the degree of

MASTER OF SCIENCE

Approved by:

Chair of Committee,	John Whitcomb
Committee Members,	Zoubeida Ounaies
	Xin-Lin Gao
Head of Department,	Dimitris Lagoudas

August 2009

Major Subject: Aerospace Engineering

ABSTRACT

Finite Element Analysis of Three-Phase
Piezoelectric Nanocomposites. (August 2009)
Kevin S. Maxwell, B.S., Texas A&M University
Chair of Advisory Committee: Dr. John Whitcomb

In recent years, traditional piezoelectric materials have been pushed to the limit in terms of performance because of countless novel applications. This has caused an increased interest in piezoelectric composites, which combine two or more constituent materials in order to create a material system that incorporates favorable attributes from each constituent. One or more of the constituents exhibits piezoelectric behavior, so that the composite has an effective electromechanical coupling. The composite material may also have enhanced properties such as stiffness, durability, and flexibility.

Finite element analyses were conducted on a three-phase piezoelectric nanocomposite in order to investigate the effects of several design parameters on performance. The nanocomposite consisted of a polyimide matrix, β-CN APB/ODPA, enhanced with single wall carbon nanotubes and PZT-5A particles. The polyimide and nanotube phases were modeled as a single homogenized phase. This results in a two-phase nanocomposite that can be modeled entirely in the continuum domain. The material properties for the nano-reinforced matrix and PZT-5A were obtained from previous experimental efforts and from the literature.

The finite element model consisted of a single representative volume element of the two-phase nanocomposite. Exact periodic boundary conditions were derived and used to minimize the analysis region. The effective mechanical, electrical, and piezoelectric properties were computed for a wide range of nanotube and PZT particle

concentrations. A discrepancy was found between the experimental results from the literature and the computational results for the effective electrical properties. Several modified finite element models were developed to explore possible reasons for this discrepancy, and a hypothesis involving dispersion of the nanotubes was formulated as an attempt to explain the difference.

The response of the nanocomposite under harmonic loading was also investigated using the finite element model. The effective properties were found to be highly dependent on the dielectric loss of the βCN/SWNT matrix. It was also found that increasing the matrix loss enhanced piezoelectric performance up to a certain point. Exploiting this type of behavior could be an effective tool in designing piezoelectric composite materials.

To my family and friends

ACKNOWLEDGMENTS

I would like to express my sincerest gratitude to my advisor, Dr. John Whitcomb, for supporting me financially and academically in both my undergaduate and graduate studies. He has patiently guided me through all of this work, and he has shown repeatedly his desire for me to succeed. His insistence on quality research has greatly impacted my studies and improved my abilities.

I would also like to thank Dr. Zoubeida Ounaies for presenting the idea for this research and agreeing to serve on my advisory committee. Without her gracious help and guidance, this work would not have been possible. I must also thank her for granting me access to experimental data from her research group, which was used extensively in this work. Her students Ricardo Perez, Amira Barhoumi, and Sujay Deshmukh were also very helpful in preparing and explaining this data.

I thank Dr. Xin-Lin Gao for taking time out of his busy schedule to serve on my advisory committee.

I thank my fellow research teammates, Brian Owens, Ross McLendon, and Julian Varghese, for their help and support in my endeavors.

I thank Dr. Gregory Odegard from Michigan Technological University for his help in understanding and interpreting some of his previous work.

I thank Clarkson Aerospace for their support in this work.

Finally, I thank my friends and family, to whom this work is dedicated, for all of their support.

TABLE OF CONTENTS

CHAPTER Page

LIST OF TABLES

LIST OF FIGURES

FIGURE Page

FIGURE Page

CHAPTER I

INTRODUCTION

A. Motivation

Piezoelectric materials have long been used in sensing and actuator applications because of their ability to couple electrical and mechanical fields. However, the performance limits of traditional piezoelectric materials have caused an increased interest in piezoelectric composites. For example, piezoelectric ceramic materials are too stiff and brittle for some applications while piezoelectric polymers are tough and flexible but lack the greater piezoelectric response of the ceramics. Traditional composite materials combine two or more constituent materials in order to create a material system that performs better than any of the constituents alone. In the case of piezoelectric composites, one or more of the constituents exhibit piezoelectric behavior, so the effective response of the composite also exhibits piezoelectric coupling. In addition, the composite material may have enhanced properties that do not directly involve coupling between electrical and mechanical fields.

There have been several attempts to create piezoelectric composite materials utilizing a polymer matrix with piezoelectric ceramic inclusions [1, 2, 3]. Ideally, this type of material system can provide the light weight and flexibility of the polymer while exhibiting a greater piezoelectric response than traditional piezoelectric polymers. The problem with such a material system is that if there is a high dielectric mismatch between the polymer and piezoelectric inclusions the material is difficult to pole. If a very large electric field is applied to the material, the polymer's low electric permittivity causes the electric field over the piezoelectric inclusions to be much

---

This thesis follows the style of Acta Materialia.

smaller than the applied field. This leads to piezoelectric inclusions that have only been partially poled, and the piezoelectric response of the composite material is quite small. Furthermore, even if the inclusions could somehow be poled completely, the low permittivity of the matrix would not allow efficient actuation of the inclusions. This is because the actuating electric field would not be able to reach the inclusions. The same problem would happen if the material was used as a sensor. A force applied to the material would cause a large electric field over the inclusions, but this electric field would remain mostly trapped in the inclusions by the low permittivity matrix.

To overcome this issue, Ounaies et al. [4, 5] have made composites consisting of a thin film polyimide matrix, piezoelectric particle inclusions, and single wall nanotubes (SWNT). The resulting nanocomposite is such that the electrical properties of the nanotubes increase the electric permittivity of the polymer matrix, so the piezoelectric particles can be poled more easily. A schematic of the three-phase nanocomposite is given in Fig. 1. The aim of this research is to investigate the effects of several design parameters for this type of material system on overall material performance.

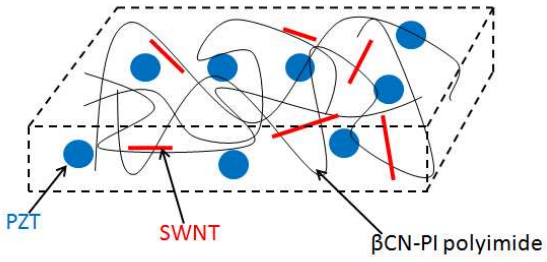

Fig. 1. Schematic of three-phase piezoelectric nanocomposite (not to scale).

B. Literature Review

There are several important areas of research that must be reviewed to fully understand the current state of knowledge for piezoelectric nanocomposites. First and foremost, the constituent dielectric properties of a piezoelectric composite play an important role in the effective electromechanical properties of the material. Therefore, the characterization of dielectric properties must be fully understood in order to predict effective piezoelectric properties. Many research groups have investigated the dielectric properties of different types of materials using experimental and computational approaches, so both methodologies will be reviewed here. In addition, research pertaining to the characterization of piezoelectric composite materials is obviously of interest in this work. Hence, separate sections are given to both experimental and computational investigations of piezoelectric composites.

1. Experimental Dielectric Properties

Ounaies et al [6] investigated the electrical properties of single wall carbon nanotube (SWNT) reinforced polyimide composites as a function of SWNT concentration. Using measured values of AC and DC conductivity, it was shown that the additions of SWNTs to the polyimide results in an effective conductivity that exhibits a percolation type behavior. Analytical and numerical models were also used in conjunction with experiment to show that bundles of nanotubes dispersed throughout the polyimide play an important role in the effective properties. A very important result of this work is the ability to tailor the electrical properties of the composite over many orders of magnitude.

Potschke et al [7, 8] used dielectric spectroscopy to measure the complex permittivity and conductivity spectra of polycarbonate (PC)/multiwalled carbon nanotube

(MWNT) composites at varying concentrations of MWNT. The frequency dependent electrical properties were used to investigate the percolation behavior and state of dispersion of the nanotubes. The percolation threshold was assumed to be the MWNT concentration where the static conductivity increased significantly. For the PC/MWNT nanocomposites, the static conductivity increased by ten orders of magnitude between 1.0 and 1.5 wt% MWNT. In addition to the static conductivity, the real and imaginary parts of complex permittivity were also found to increase significantly above the percolation threshold.

The dispersion of the nanotubes was investigated by varying processing parameters such as mixing screw speed and mixing time. The permittivity and conductivity spectra from the resulting composites indicated that the percolation, and therefore dispersion, of the nanotubes is highly dependent on processing. Higher screw speeds at longer mixing times generally resulted in percolation at lower concentrations of MWNTs, which indicated better overall dispersion of the nanotubes.

Youngs [9] performed dielectric measurements on samples consisting of silver coated microspheres in a paraffin wax matrix, and a clear percolation transition was observed at higher inclusion fractions. The results were also compared to several effective medium and percolation theories. Effective mean theories such as Bruggeman and Maxwell-Garnett failed to predict effective permittivity for volume fractions greater than 0.1. However, the Kirkpatrick-Zallen and McLachlan statistical percolation theories were able to provide a good fit for filler fraction dependence of permittivity.

2. Modeling of Dielectric Properties

Krakovsky et al [10] modeled the dielectric properties of two-dimensional composites using the finite element method. Interfacial, or Maxwell-Wagner-Sillars polarization

was the only polarization mechanism considered so that the material permittivities were frequency independent. The constituent phases of the composites consisted of two different materials with complex permittivities, and the dielectric losses were assumed to be purely ohmic. The dielectric spectra obtained from FEA were compared to results obtained using mixture formulas. The FEA spectra were found to lie between the curves given by the Maxwell-Garnett and Bruggeman formulas. It was also found that the FEA spectra for a random composite differed from the spectra for a periodic composite.

Sareni et al [11] modeled the complex effective permittivity of a lossy composite material using FEA. The finite element method was found to be an accurate way to calculate the permittivity of this type of material in the quasistatic limit. The results were also compared to the Bergman and Milton theory, and the two methods were found to be consistent.

Ang et al [12] calculated the effective permittivity and loss of two-phase composites using FEA. The inclusion phase of the composite was modeled as various shapes such as circles, triangles, and rings. It was found that given a fixed volume fraction, the shape of the inclusion affects the electric field distribution enough to greatly affect the effective permittivity. Zhang et al. [13] performed a nonlinear finite element analysis on a PZT/polymer composite to understand the poling behavior of these types of composites. The effects of poling voltages and PZT volume fraction on the distribution of residual stress in the PZT were studied. It was found that under a certain PZT volume fraction, poling caused a residual compressive stress on the inclusions that partially depolarized the PZT.

Wu et al [14] used a finite-difference time-domain (FDTD) method to analyze the effective dielectric properties of three-dimensional composite materials. They found that the inclusion shape, inclusion concentration, and operating frequency can all

have significant effects on a composite material's electrical properties.

3. Experimental Piezoelectric Composites

Researchers over the last several decades have synthesized many types of piezoelectric composites. Safari et al. [3] made piezoelectric composites by dispersing $PbTiO_3$ powder in a dielectric gel polymer. Measurements of the resulting composites yielded a usable piezoelectric response with d_{33} values as high as 60 pC/N, which is greater than that of PVDF. Liu et al. [1] made lead zirconate titanate (PZT)/PVC composites doped with semiconducting graphite particles. The graphite allowed more effective poling of the PZT inclusions by increasing the amount of electric field over the PZT. However, the highest d_{33} value measured was approximately 22 pC/N, which is about the same as PVDF. Showcasing a novel application of piezoelectric composites, White et al. [15] developed a piezoelectric ceramic/polymer composite that can be used as a thick film strain sensor for vibration monitoring of structures. The composite is produced as a paint which can be applied using conventional paint spraying equipment.

Hori et al. [16] developed piezoelectric composites consisting of PZT/carbon black/epoxy. Instead of pure piezoelectric response, their goal was to create an elastic damping material with a large effective mechanical loss factor. The resulting piezoelectric composite converted mechanical vibrations to alternating electrical energy, which were then dissipated by joule heating through the network of carbon black particles and an external resistor. By increasing the amount of carbon black in the composite, they were able to increase the piezoelectric loss of the material, which allowed the material to dissipate mechanical energy more efficiently. Similarly, Tian and Wang [17] prepared and investigated samples of an epoxy/multiwall carbon nanotube (MWNT)/PZT piezoelectric nanocomposite. Like the carbon black that Hori

et al. used, the MWNTs formed a network throughout the material that allowed the composite to dissipate energy. These composite systems are a promising type of damping material, and their enhanced dielectric properties indicate that the addition of carbon black or MWNTs can facilitate better poling.

4. Modeling of Piezoelectric Composites

There has also been much interest in modeling the response of piezoelectric composites because an accurate model could help design a material system before ever spending time and money to make a test specimen. Shin [18] modeled PZT/polymer composites using finite element analysis (FEA), but the available computing power at the time limited the models to a very small number of elements, which resulted in low accuracy. However, an interesting result from the analysis was the fact that the hydrostatic piezoelectric charge coefficients only increased with increasing PZT content up to a certain point. After this, the hydrostatic coefficients actually decreased with increasing PZT content. This observation implies that there is an optimum PZT volume fraction for which the hydrostatic piezoelectric response is maximized. Salehi-Khojin and Jalili [19] attempted to design piezoelectric polymer composites with tunable mechanical properties ranging from a stiff structure to an efficient mechanical damper. They modeled the composites using a shear-lag model, and they found that stiffer structures show better tuning capabilities. These types of materials could be used in the next generation of active vibration damping systems.

Sherrit and Mukherjee [20] extended the idea of complex permittivity to the use of complex material constants for piezoelectric materials. They gave various reasons for using complex dielectric, elastic, and piezoelectric coefficients to account for the losses that arise when piezoelectric materials are subjected to harmonic loads. In addition, Lamberti et al. [21] extended the definition of the electromechanical coupling factor

to include losses in the context of a complex factor. Along the same lines, Piquette and McLaughlin [22] were able to come up with completely real coupling factors while keeping all other material constants complex.

Odegard [23] used FEA to predict the effective properties of several types of piezoelectric polymer composites. The four types of composites modeled were a graphite/poly(vinylidene fluoride) (PVDF) composite, a silicon carbide (SiC)/PVDF particulate composite, a fibrous lead zirconate titanate (PZT)/polyimide composite, and a PZT/polyimide particulate composite. The FEA results were compared to predictions from Mori-Tanaka and self-consistent methods, as well as a new, proposed model. The FEA data was used as a benchmark to show that the proposed micromechanics model could predict properties more accurately than the Mori-Tanaka and self-consistent schemes.

Silva et al [24] used FEA along with sequential linear programming (SLP) to find optimized unit cell topologies for piezoelectric composites. The linear programming was used to find the distribution of phases that optimizes the performance characteristics of the composite material. The effective properties for each distribution were found using FEA applied to a unit cell subject to periodic boundary conditions. The microstructures obtained from the optimization process showed a large increase in performance when compared to both pure piezoelectric material and more simplistic types of unit cells. The work highlights the ability to engineer a composite piezoelectric material to obtain better performance characteristics.

Berger el at [25] modeled piezoelectric fiber composites consisting of PZT fibers embedded in a soft polymer matrix. Effective coefficients for the composite were calculated using the asymptotic homogenization method (AHM) and FEA. Periodic boundary conditions were applied to the representative volume element used in the FEA model. The results from the AHM and FEA models were compared, and it

was found that the two analysis methods compared reasonably well with each other, especially at lower volume fractions of PZT. The differences between the two methods was attributed to the AHM assuming transverse isotropy of the composite while the FEA model used a square packing of fibers.

Kelly et al [26] investigated the effects of loss in piezoelectric materials. The main contributors to loss were identified as DC conductivity, dielectric loss, acoustic viscosity, and piezoelectric loss. They argued that all forms of loss can be lumped into the electromechanical coupling factor, which results in a complex value.

C. Scope of Research

The overall objectives of this research were to develop a micromechanics model of a three-phase piezoelectric nanocomposite, such as the one shown in Fig. 1, that can predict effective properties and to investigate the effects of several design parameters on performance. Finite element analysis was used to solve the micromechanics boundary value problem. The effects of various parameters on electrical and piezoelectric performance were explored in several parametric studies in an attempt to improve performance and enhance understanding of the design criteria for a piezoelectric composite. The finite element modeling was performed with COMSOL Multiphysics [27] because this software has the ability to model coupling between a wide array of physical fields. Thus, COMSOL is well suited to the peculiarities of modeling the electromechanical coupling in a piezoelectric material. Also, COMSOL allows the use of scripting, and this feature was used extensively to efficiently perform parametric studies.

Parametric studies were performed to determine the effective electromechanical properties of a piezoelectric composite under static electromechanical loads. In the

first study, material properties of a two-phase piezoelectric microcomposite from [23] were used, and the properties obtained were compared to results in that work. This gave some validation to the modeling approach used. Additionally, predicted properties were compared to several sets of experimental results, and good agreement between the results was observed. A second parametric study was then performed using the material properties of the three-phase nanocomposite from [5]. The results were compared to experimental results when possible so that the accuracy of the model could be quantified. The results did not initially agree well with experimental values, so an attempt was made to understand the discrepancy.

Because many applications of piezoelectric material systems involve harmonic excitation over a broad frequency spectrum, a parametric study of harmonic behavior was also performed on the three-phase nanocomposite. The finite element analysis was performed in the frequency domain with complex-valued material properties, which represent the response of the material at all excitation frequencies. From this, the complex-valued effective properties were calculated and compared to other types of piezoelectric materials. It is hoped that, along with the predictions of static effective properties, the complex effective properties for the three-phase nanocomposite will contribute to the overall understanding of this material system. In particular, the results will hopefully show that the addition of carbon nanotubes to the composite matrix provides a logical way to increase piezoelectric performance.

CHAPTER II

THEORY

A. Piezoelectric Effect

The piezoelectric effect is a property of certain materials that manifests itself as a coupling between electrical and mechanical fields [28]. If a mechanical stress is applied to the material, an electric displacement results, and the application of an electric field results in a mechanical strain. The mechanical-to-electrical coupling is termed the direct piezoelectric effect because it was discovered first. The electrical-to-mechanical coupling was observed later and was thus coined the inverse or converse piezoelectric effect. Both effects occur because of the presence of electric dipoles within the material.

B. Governing Equations

In order to solve an elasticity boundary value problem, there are four types of governing equations that must be considered. They are equilibrium, kinematic relations, constitutive relations, and boundary conditions. This can be extended to solving a piezoelectric boundary value problem by combining the governing equations from elasticity and electrostatics. The result is a system of coupled partial differential equations that can be organized into four groups of equations. The groups are divergence equations, gradient equations, constitutive relations, and boundary conditions.

1. Divergence Equations

There are two divergence equations that govern piezoelectric materials. The first is the equilibrium equation of elasticity as given in Equation 2.1 below, where T_{ij} is

the stress tensor and F_i are body forces. The second is the well known Gauss's Law of electrostatics. Gauss's Law is given in Equation 2.2 where D_i is the electric field vector, and ρ_f is the free electric charge density.

$$\frac{\partial T_{ij}}{\partial x_j} + F_i = 0 \tag{2.1}$$

$$\frac{\partial D_i}{\partial x_j} = \rho_f \tag{2.2}$$

In this work there are never any body forces or free charge densities. Therefore, the equilibrium equation and Gauss's Law simplify to

$$\frac{\partial T_{ij}}{\partial x_j} = 0 \tag{2.3}$$

$$\frac{\partial D_i}{\partial x_j} = 0. \tag{2.4}$$

2. Gradient Equations

The gradient equations for piezoelectricity are the strain-displacement or kinematic relations from elasticity and the definition of electric field from electrostatics, which are given in Equations 2.5 and 2.6, respectively. In the equations, S_{ij} is the strain tensor, u_i is the displacement vector, and V is the electric field potential.

$$S_{ij} = \frac{1}{2}\left(\frac{\partial u_i}{\partial x_j} + \frac{\partial u_j}{\partial x_i}\right) \tag{2.5}$$

$$E_i = -\frac{\partial V}{\partial x_i} \tag{2.6}$$

3. Constitutive Relations

The constitutive equations for a piezoelectric material are given in Equation 2.7 where s^E_{ijkl} is the constant electric field compliance tensor, T_{ij} is the Cauchy stress tensor, ε^T_{ij} is the stress-free electric permittivity tensor, and d_{ijk} is the piezoelectric coupling

tensor. Note that if $d_{ijk} = 0$, the constitutive equations reduce to the constitutive equations of elasticity and electrostatics.

$$S_{ij} = s^E_{ijkl} T_{kl} + d_{lij} E_l$$
$$D_i = d_{ikl} T_{kl} + \varepsilon^T_{il} E_l \tag{2.7}$$

The constitutive relations in tensor notation can be tedious to use. Therefore, from this point forward, the constitutive relations will be expressed in contracted, matrix notation. With this notation, the constitutive relations become

$$\mathbf{S} = s^E \mathbf{T} + d\mathbf{E}$$
$$\mathbf{D} = d'\mathbf{T} + \varepsilon^T \mathbf{E}, \tag{2.8}$$

where a primed matrix denotes the transpose of the matrix.

The superscripts on s^E and ε^T indicate that the material properties depend on boundary conditions. The superscripts E and D represent constant electric field and constant electric displacement boundary conditions, respectively. The superscripts T and S indicate stress-free and strain-free boundary conditions, respectively. To understand the meaning of the different electrical and mechanical boundary conditions, consider the piezoelectric material specimen in Fig. 2. There are electrodes on both ends of the specimen, and a switch between the electrodes allows the electrical boundary condition to be switched from open to closed circuit.

If the compliance of the material is to be measured, a known stress is applied and the resulting strain is measured. If the stress is applied with a short circuit electrical boundary condition, the electric field across the specimen is zero, and the constitutive

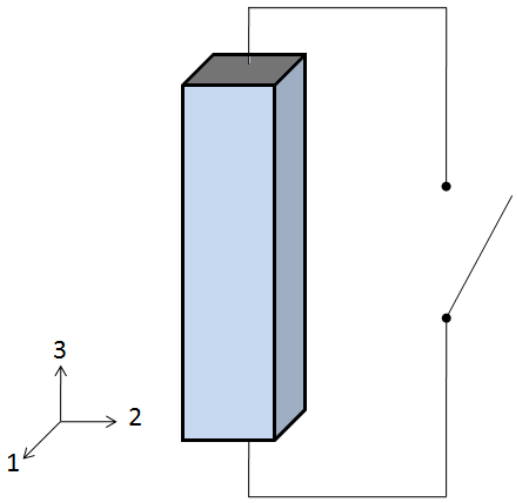

Fig. 2. Piezoelectric material with electroded ends subject to applied stress and electric fields in the 3-direction.

relation reduces to

$$\mathbf{S} = s^E\mathbf{T}$$
$$\mathbf{D} = d'\mathbf{T}. \tag{2.9}$$

However, if the stress is applied with an open circuit boundary condition, the electric displacement across the specimen is zero, and the constitutive relation becomes

$$\mathbf{S} = s^E\mathbf{T} + d\mathbf{E} \tag{2.10}$$
$$0 = d'\mathbf{T} + \varepsilon^T\mathbf{E}. \tag{2.11}$$

Rearranging Equation 2.11, we obtain

$$\mathbf{E} = -(\varepsilon^T)^{-1}d'\mathbf{T}, \tag{2.12}$$

which can be substituted into Equation 2.10 to obtain

$$\begin{aligned}\mathbf{S} &= s^E\mathbf{T} - d(\varepsilon^T)^{-1}d'\mathbf{T} \\ &= \left(s^E - d(\varepsilon^T)^{-1}d'\right)\mathbf{T},\end{aligned} \tag{2.13}$$

where the actual compliance for the open circuit, constant electric displacement boundary condition is clearly given by

$$s^D = s^E - d(\varepsilon^T)^{-1}d' \tag{2.14}$$

Similarly, the mechanical boundary conditions affect the electric properties of a piezoelectric material. Consider again the piezoelectric specimen in Fig. 2. This time we want to measure the electric permittivity of the material. A known electric field, E, is applied, and the resulting electric displacement, D, is somehow measured. If, during the application of E, the specimen is allowed to freely deform, then the stresses, $\mathbf{T}$ in the specimen will be zero. The constitutive relation reduces to

$$\begin{aligned}\mathbf{S} &= d\mathbf{E} \\ \mathbf{D} &= \varepsilon^T\mathbf{E}.\end{aligned} \tag{2.15}$$

However, if the electric field is applied while the specimen is mechanically constrained in all directions, the strains in the specimen are zero, and the constitutive relation becomes

$$0 = s^E\mathbf{T} + d\mathbf{E} \tag{2.16}$$

$$\mathbf{D} = d'\mathbf{T} + \varepsilon^T\mathbf{E}. \tag{2.17}$$

Rearranging Equation 2.16, we obtain

$$\begin{aligned}\mathbf{T} &= -(s^E)^{-1} d\mathbf{E} \\ &= -c^E d\mathbf{E},\end{aligned} \tag{2.18}$$

which is substituted into Equation 2.17 to obtain

$$\begin{aligned}\mathbf{D} &= \varepsilon^T \mathbf{E} - d' c^E d\mathbf{E} \\ &= \left(\varepsilon^T - d' c^E d\right) \mathbf{E},\end{aligned} \tag{2.19}$$

where the actual permittivity for the strain-free boundary condition, ε^S, is clearly given by

$$\varepsilon^S = \varepsilon^T - d' c^E d \tag{2.20}$$

The form of the constitutive relations given in Equation 2.8 is usually referred to as the strain-charge form. This is the form most piezoelectric material vendors use to specify material properties. However, sometimes it is desirable to use other forms that have different independent variables. Another widely used form is the stress-charge form which is given in Equation 2.21. In the stress-charge form, c^E is the constant electric field stiffness tensor, ε^S is the strain-free electric permittivity, and e is the piezoelectric coupling tensor.

$$\begin{aligned}\mathbf{T} &= c^E \mathbf{S} - e\mathbf{E} \\ \mathbf{D} &= e'\mathbf{S} + \varepsilon^S \mathbf{E},\end{aligned} \tag{2.21}$$

It should be stressed that both constitutive forms are equivalent. The use of a particular form is dictated by which independent variables lend themselves to a particular analysis. For example, the implementation of periodic boundary conditions in COMSOL makes the stress-charge form a good choice for post processing the results

from analyses in this work. This is because the periodic boundary conditions are expressed in terms of volume average strains and volume average electric fields, and it is easier to calculate the effective material properties if the constitutive form is also in terms of strains and electric fields. To illustrate the structure of the matrices in the constitutive relations, the expanded form of the stress-charge constitutive relations is given in Equation 2.22 using the standard Voight notation.

$$\begin{Bmatrix} T_{11} \\ T_{22} \\ T_{33} \\ T_{12} \\ T_{23} \\ T_{13} \end{Bmatrix} = \begin{bmatrix} c_{11} & c_{12} & c_{13} & 0 & 0 & 0 \\ c_{12} & c_{22} & c_{23} & 0 & 0 & 0 \\ c_{13} & c_{23} & c_{33} & 0 & 0 & 0 \\ 0 & 0 & 0 & c_{44} & 0 & 0 \\ 0 & 0 & 0 & 0 & c_{55} & 0 \\ 0 & 0 & 0 & 0 & 0 & c_{66} \end{bmatrix} \begin{Bmatrix} S_{11} \\ S_{22} \\ S_{33} \\ 2S_{12} \\ 2S_{23} \\ 2S_{13} \end{Bmatrix} - \begin{bmatrix} 0 & 0 & e_{13} \\ 0 & 0 & e_{23} \\ 0 & 0 & e_{33} \\ 0 & e_{24} & 0 \\ e_{15} & 0 & 0 \\ 0 & 0 & 0 \end{bmatrix} \begin{Bmatrix} E_1 \\ E_2 \\ E_3 \end{Bmatrix}$$

$$\begin{Bmatrix} D_1 \\ D_2 \\ D_3 \end{Bmatrix} = \begin{bmatrix} 0 & 0 & 0 & 0 & e_{15} & 0 \\ 0 & 0 & 0 & e_{24} & 0 & 0 \\ e_{13} & e_{23} & e_{33} & 0 & 0 & 0 \end{bmatrix} \begin{Bmatrix} S_{11} \\ S_{22} \\ S_{33} \\ 2S_{12} \\ 2S_{23} \\ 2S_{13} \end{Bmatrix} + \begin{bmatrix} \varepsilon_{11} & 0 & 0 \\ 0 & \varepsilon_{22} & 0 \\ 0 & 0 & \varepsilon_{33} \end{bmatrix} \begin{Bmatrix} E_1 \\ E_2 \\ E_3 \end{Bmatrix} \tag{2.22}$$

4. Boundary Conditions

The boundary conditions for the piezoelectric boundary value problem can be split into natural and essential boundary conditions. The natural boundary conditions are given in Equation 2.23 while the essential boundary conditions are given in Equation 2.24. The terms with a '^' are specified values. Note that for the natural boundary

conditions, $\hat{t}_i$ are applied tractions, and $\hat{q}$ is applied charge.

$$T_{ij}n_j = \hat{t}_i$$
$$D_i n_i = \hat{q} \tag{2.23}$$

$$u_i = \hat{u}_i$$
$$V = \hat{V} \tag{2.24}$$

C. Finite Element Method

The finite element software COMSOL Multiphysics was used for all of the finite element modeling in this work. This software was chosen because it allows the finite element method to be applied to solving a general set of partial differential equations. In addition, there is a piezoelectric material module already defined, and the software also supports solving problems in the frequency domain. Another important feature of COMSOL is the implementation of periodic boundary conditions, which are necessary for micromechanical analysis.

COMSOL solves the weak form of the governing partial differential equations. To obtain the weak form of the elasticity equations, start with the equilibrium equations

$$\frac{\partial T_{ij}}{\partial x_j} + F_i = 0, \tag{2.25}$$

and multiply by a test function δu_i. Then integrate over the volume domain (Ω).

$$\int_\Omega \left(\frac{\partial T_{ij}}{\partial x_j} + F_i \right) d\Omega = 0 \tag{2.26}$$

Now integrate by parts to obtain

$$\int_\Gamma \delta u_i T_{ij} n_j d\Gamma + \int_\Omega \left(\delta u_i F_i - \frac{\partial \delta u_i}{\partial x_j} T_{ij} \right) d\Omega = 0, \tag{2.27}$$

where Γ is a surface domain. Rearranging, we get

$$\int_\Gamma \delta u_i T_{ij} n_j d\Gamma + \int_\Omega \delta u_i F_i d\Omega - \int_\Omega \frac{\partial \delta u_i}{\partial x_j} T_{ij} d\Omega = 0. \tag{2.28}$$

The kinematic relations can now be used to obtain

$$\int_\Gamma \delta u_i T_{ij} n_j d\Gamma + \int_\Omega \delta u_i F_i d\Omega - \int_\Omega \delta S_{ij} T_{ij} d\Omega = 0, \tag{2.29}$$

which is equivalent to the weak form that COMSOL solves for elasticity using finite elements.

To obtain the weak form of the electrostatics equations, start with Gauss's Law

$$\frac{\partial D_i}{\partial x_j} - \rho_f = 0, \tag{2.30}$$

and multiply by a test function δV. Then integrate over the domain to obtain

$$\int_\Omega \delta V \left(\frac{\partial D_i}{\partial x_j} - \rho_f \right) d\Omega = 0. \tag{2.31}$$

Integration by parts yields

$$\int_\Gamma \delta V D_i n_i d\Gamma + \int_\Omega \left(-\delta V \rho_f - \frac{\partial \delta V}{\partial x_i} D_i \right) d\Omega = 0. \tag{2.32}$$

Rearranging, we get

$$\int_\Gamma \delta V D_i n_i d\Gamma - \int_\Omega \delta V \rho_f d\Omega - \int_\Omega \frac{\partial \delta V}{\partial x_i} D_i d\Omega = 0. \tag{2.33}$$

Recall that the definition of electric field is given by

$$E_i = -\frac{\partial V}{\partial x_i}. \tag{2.34}$$

This can be used in the weak form to obtain

$$\int_\Gamma \delta V D_i n_i d\Gamma - \int_\Omega \delta V \rho_f d\Omega - \int_\Omega \delta E_i D_i d\Omega = 0, \tag{2.35}$$

which is equivalent to the weak form COMSOL solves for electrostatics using finite elements.

D. Harmonic Analysis

Dynamic material properties are important for piezoelectric materials because many applications require piezoelectrics to be used over a broad frequency range. In order to model this type of behavior using finite elements, a framework must be set up to allow efficient calculation of dynamic effective properties.

1. Circuit Analogs

Lossy dielectric materials are important for the βCN-PI/SWNT/PZT material system because the addition of conductive nanotubes to the polymer matrix causes the matrix to behave as a lossy material under alternating current (AC) loads. A lossy material is a material that somehow dissipates electromagnetic energy passing through it. Note that all real materials are lossy to some extent, but in many materials the loss can be considered negligible. However, the βCN-PI/SWNT matrix is lossy enough that significant changes in effective properties occur under alternating current conditions.

The easiest way to understand the effect of harmonic excitations on a dielectric material is to use an electrical circuit analog that represents the material [29]. The well-defined AC circuit analysis methods from electrical engineering can then be used to understand material behavior. For example, a lossless dielectric material can be represented by a simple capacitor. In order to understand and analyze a circuit analog, several material parameters must be defined. Many of the electrical engineering equations and derivations are taken from [30, 31].

Ohm's Law, which governs the macroscopic relationship between resistance R,

voltage V, and current I in electrical elements, is given as

$$R = \frac{\Delta V}{I}. \tag{2.36}$$

The resistivity ρ of a material is defined through the constitutive relation

$$E = \rho J, \tag{2.37}$$

where E is electric field and J is current density. If the material considered is formed into a cylindrical material specimen with electrodes placed at the ends, the relationship between E and J of the specimen becomes

$$\frac{\Delta V}{d} = \rho \frac{I}{A}, \tag{2.38}$$

where ΔV is the potential difference between the electrodes, I is the current across the specimen, A is the cross sectional area of the electrodes, and d is the distance between the electrodes.

The resistivity ρ of the specimen is then

$$\rho = \frac{\Delta V A}{I d}. \tag{2.39}$$

We know from Ohm's Law that the factor $\Delta V/I$ is equal to the resistance R. The resistivity becomes

$$\rho = R \frac{A}{I d}. \tag{2.40}$$

Now the conductivity of the same material specimen can be defined as the reciprocal of the resistivity as follows

$$\sigma = \frac{1}{\rho} = \frac{d}{RA}. \tag{2.41}$$

Another parameter that must be defined is capacitance. If the voltage potential between two conductors is kept constant at ΔV, then a charge Q will form on each

conductor proportional to ΔV. The proportionality constant is capacitance

$$Q = C\Delta V \tag{2.42}$$

In order to define the capacitance of a material between two parallel electrodes, Gauss's Law is used to find the electric field between the electrodes

$$E = \frac{q}{\varepsilon A} \tag{2.43}$$

Setting $q = Q$ and substituting Equation 2.42 into Equation 2.43, we get the capacitance for the material between the parallel plates

$$C = \frac{A\varepsilon}{d}. \tag{2.44}$$

A very important parameter in AC circuit analysis is impedance. Impedance can be thought of as a complex resistance, but several concepts must be introduced in order to properly define it. Consider a linear electrical element subject to a harmonic current I that can be represented as

$$I = I_0 e^{j\omega t}, \tag{2.45}$$

where I_0 is a real valued amplitude, ω is the radial frequency of the signal, and j is $\sqrt{-1}$.

Now assume that the driving current produces a harmonic potential difference V across the element which can be measured and represented as

$$V = V_0 e^{j(\omega t+\phi)}, \tag{2.46}$$

where ϕ is the phase shift between the two harmonic signals V and I. Note that the frequencies of the signals are the same because the element is assumed to be linear.

The impedance Z of the electrical element can now be defined as the ratio of V

and I as shown in Equation 2.47.

$$\begin{aligned} Z &= \frac{V}{I} \\ &= \frac{V_0 e^{j(\omega t+\phi)}}{I_0 e^{j(\omega t)}} \\ &= \frac{V_0}{I_0} e^{j\phi} \\ &= |Z| e^{j\phi} \end{aligned} \tag{2.47}$$

As can be seen in Equation 2.47, impedance is simply a complex number that relates V and I. The form of impedance given in the equation is called the polar form, but it is usually expressed in the rectangular form:

$$Z = Z' + jZ'', \tag{2.48}$$

where

$$\begin{aligned} Z' &= |Z| cos\phi \\ Z'' &= |Z| sin\phi. \end{aligned} \tag{2.49}$$

The principle of complex impedance can now be used to analyze a material circuit analog. The goal of the analysis is to obtain the effective permittivity that can represent the circuit analog, which can then be used to describe the frequency response of the material. When considering a lossy dielectric material, the most widely used circuit is the parallel RC circuit [29]. This circuit consists of a perfect resistor and a perfect capacitor connected in parallel, and a schematic is shown in Fig. 3 below. The effective impedance of two elements connected in parallel is given as

$$\frac{1}{Z_{eff}} = \frac{1}{Z_1} + \frac{1}{Z_2}. \tag{2.50}$$

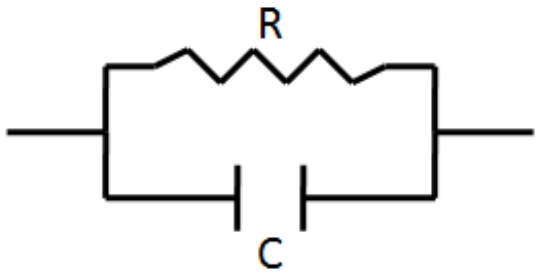

Fig. 3. Schematic diagram of parallel RC circuit.

The impedance of a resistor is simply the resistance of the resistor, as shown in Equation 2.51.

$$Z_R = R \tag{2.51}$$

The impedance of a capacitor is

$$Z_C = \frac{1}{j\omega C} = -\frac{j}{\omega C}. \tag{2.52}$$

Substituting the impedances of a capacitor and resistor into the effective impedance given in Equation 2.50, we get the effective impedance relation of the parallel RC circuit given in Equation 2.53.

$$\begin{aligned} \frac{1}{Z_{eff}} &= \frac{1}{R} + \frac{1}{\frac{1}{j\omega C}} \\ &= \frac{1}{R} + j\omega C \end{aligned} \tag{2.53}$$

If we assume that there is lossy capacitor that is equivalent to the RC circuit, then there must be an effective capacitance C_{eff} of the RC circuit, and C_{eff} is related to the effective impedance of the RC circuit. Therefore, the capacitive impedance

relation given in Equation 2.52 can be extended to mean

$$Z_{eff} = \frac{1}{j\omega C_{eff}} = -\frac{j}{\omega C_{eff}}. \tag{2.54}$$

Substituting Equation 2.54 into Equation 2.53, we obtain

$$j\omega C_{eff} = \frac{1}{R} + j\omega C. \tag{2.55}$$

Substituting the definition of capacitance from Equation 2.44 yields

$$j\omega \frac{A\varepsilon_{eff}}{d} = \frac{1}{R} + j\omega \frac{A\varepsilon'}{d}, \tag{2.56}$$

where ε_{eff} is the effective permittivity of the circuit. Rearranging, we obtain

$$\varepsilon_{eff} = \frac{d}{j\omega RA} + \varepsilon'. \tag{2.57}$$

Finally, the definition of conductivity from Equation 2.41 is substituted to obtain the effective, frequency dependent permittivity of the parallel RC circuit, as given in Equation 2.58.

$$\varepsilon_{eff} = \varepsilon' - j\varepsilon'' = \varepsilon' - j\frac{\sigma}{\omega} \tag{2.58}$$

2. Harmonic Analysis Using Complex Numbers

Although the parallel RC circuit analog is very helpful in gaining an understanding of harmonically excited dielectric materials, there are problems with assuming such a response. Sherrit and Mukherjee [20] explained that in most piezoelectric ceramic materials, the complex permittivity is due to a polarization lag rather than a leakage current due to Ohmic conduction. Using an RC circuit to model complex permittivity, however, assumes that the imaginary part of permittivity is due entirely to Ohmic conduction, and it also imposes an inverse relationship between the imaginary part of permittivity and frequency [32]. This inverse relationship is not necessarily present

in piezoelectric materials.

In order to avoid these problems, there is a much more general way to interpret and model the response of a lossy dielectric. Consider the harmonic electric field E that can be represented as

$$E = E_0 e^{j\omega t}. \tag{2.59}$$

If E is applied to a dielectric material, a harmonic electric displacement D of the same frequency will develop in the material according to the electrostatic constitutive relation $D = \varepsilon E$. If the material is a lossy dielectric, the waveform of D will be of the same frequency as E, but it will lag the driving electric field by an angle ϕ.

$$D = D_0 e^{j(\omega t+\phi)} \tag{2.60}$$

Using the constitutive relation for a dielectric material, the material's electric permittivity can be defined as

$$\begin{aligned} \varepsilon &= \frac{E}{D} \\ &= \frac{E_0 e^{j(\omega t)}}{D_0 e^{j(\omega t+\phi)}} \\ &= \frac{E_0}{D_0} e^{-j\phi} \\ &= \frac{E_0}{D_0} cos(\phi) - j\frac{E_0}{D_0} sin(\phi). \end{aligned} \tag{2.61}$$

The complex permittivity is usually generalized with the following notation [29, 33].

$$\varepsilon = \varepsilon' - j\varepsilon'' \tag{2.62}$$

At this point it must be emphasized that there have been no assumptions made about the dependence of permittivity on frequency or conductivity. A complex valued permittivity is simply assumed and can be calculated by applying an electric field to

a material, measuring the electric displacement response, and finding the complex ratio between the two. Hippel [32] showed that using a complex permittivity instead of an RC circuit ensures that no incorrect assumptions are made about the frequency response of a dielectric material. Of course, it is still implicitly assumed that the input and response both have the same frequency.

3. Complex Piezoelectric Material Properties

A lossy dielectric material is modeled with a complex permittivity value. As was seen in the previous section, a non-zero imaginary part of permittivity indicates there is a phase lag between the driving electric field E and the resulting electric displacement D. A simple examination of the piezoelectric constitutive relation in Equation 2.22 reveals that if the permittivity ε_{11} is complex, the only value that necessarily becomes complex is D_1. However, in the case of a composite where the matrix has a complex permittivity, and the piezoelectric inclusion has all real-valued material properties, it will be shown in the results that all of the effective material properties become complex.

All realistic materials have some mechanical loss associated with them. Similarly, all piezoelectric materials have some piezoelectric loss associated with the piezoelectric coefficients of the material. However, these intrinsic losses are assumed to be zero in this work because experimental values for them were unavailable. Therefore, the complex effective stiffness and piezoelectric coefficients that result from having a composite material with a lossy dielectric matrix are due solely to the lossy permittivity value.

E. Electromechanical Coupling Factor

The electromechanical coupling factor is a dimensionless quantity that material scientists use to quantify the electromechanical energy conversion in piezoelectric materials. It is a combination of specific elastic, dielectric, and piezoelectric coefficients. Equation 2.63 gives the most common definition of the coupling factor k_{ij}.

$$k_{ij} = \sqrt{\frac{d_{ij}^2}{\varepsilon_{ii}^T s_{jj}^E}} \tag{2.63}$$

The following is based on derivations of the coupling factor from [28] and [21]. Note that the coupling factor can be derived from either the direct or converse piezoelectric effects.

1. Direct Piezoelectric Effect

Consider a block of piezoelectric material like the one in Fig. 4. The ends of the specimen are electroded, and the electrical boundary condition at the ends can be switched between open and closed (short) circuit. A mechanical stress $\bar{T}_3$ is incrementally applied to the material while the electric terminals are shorted ($E_3 = 0$). This causes the transition from Point 1 to Point 2 on the $S - T$ diagram in Fig. 5. Note that only the response in the 3-direction will be considered.

Because $E_3 = 0$, the constitutive relations for the transition from Point 1 to Point 2 reduce to

$$\begin{aligned} S_3 &= s_{33}^E T_3 \\ D_3 &= d_{33} T_3. \end{aligned} \tag{2.64}$$

An inspection of Equation 2.64 reveals that the slope of the line from Point 1 to Point 2 on the S-T diagram is equal to s_{33}^E, the short circuit (zero electric field) com-

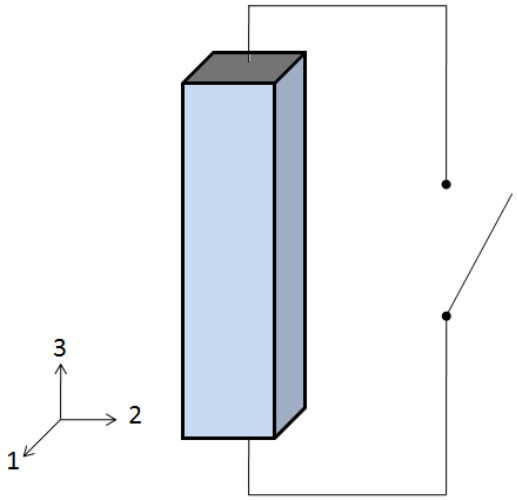

Fig. 4. Piezoelectric material with electroded ends subject to applied stress and electric fields in the 3-direction.

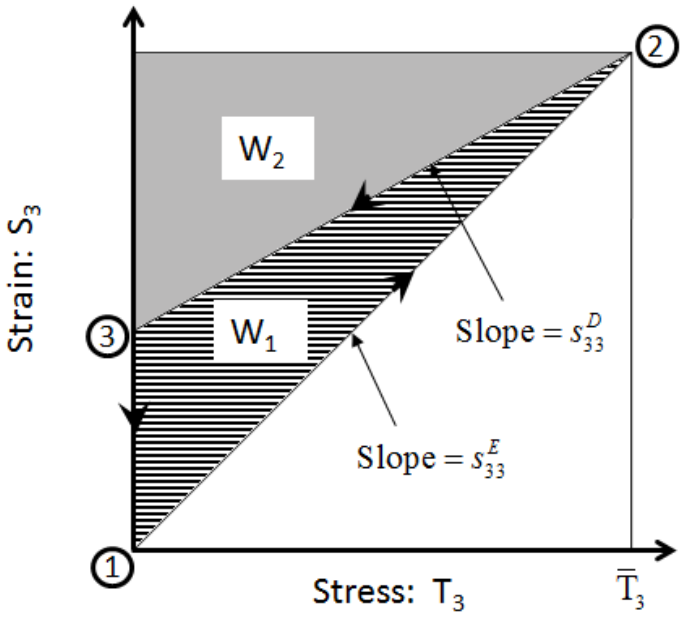

Fig. 5. Graphical interpretation of the mechanical to electrical cycle for the coupling factor k_{33}.

pliance. The total mechanical energy density applied to the specimen is proportional to the area $W_1 + W_2$. When the stress reaches $\bar{T}_3$ at Point 2 the electrical boundary condition is changed to an open circuit. This causes the electric displacement in the specimen to remain constant at the value $\hat{D}_3$ given in Equation 2.65.

$$\hat{D}_3 = d_{33}\bar{T}_3 \tag{2.65}$$

The stress is now incrementally reduced to its initial value (Points 2-3). The constitutive relations for this part of the cycle are given in Equation 2.66, where the electric displacement is held constant.

$$\begin{aligned} S_3 &= s_{33}^E T_3 + d_{33} E_3 \\ \hat{D}_3 &= d_{33}\bar{T}_3 = d_{33} T_3 + \varepsilon_{33}^T E_3 \end{aligned} \tag{2.66}$$

From the second constitutive relation, we know E_3:

$$E_3 = \frac{\hat{D}_3 - d_{33} T_3}{\varepsilon_{33}^T}. \tag{2.67}$$

Substituting E_3 back into the first part of the constitutive relation, we get:

$$\begin{aligned} S_3 &= s_{33}^E T_3 + d_{33}\left(\frac{\hat{D}_3 - d_{33} T_3}{\varepsilon_{33}^T}\right) \\ &= \left(s_{33}^E - \frac{d_{33}^2}{\varepsilon_{33}^T}\right) T_3 + d_{33}\frac{\hat{D}_3}{\varepsilon_{33}^T} \\ &= s_{33}^D T_3 + d_{33}\frac{\hat{D}_3}{\varepsilon_{33}^T}. \end{aligned} \tag{2.68}$$

Equation 2.68 shows that the line between Points 2 and 3 has a slope equal to s_{33}^D, the open circuit (zero electric displacement) compliance. The relation also indicates that the line does not pass through the origin on the S-T plot. This transition reduces the mechanical energy density in the specimen to the area W_1.

At this point there is still some residual strain leftover in the material, so an ideal electrical load is connected at Point 3 which decreases the strain to its initial value at Point 1 which completes the cycle. The work done on the ideal electrical load is represented by the area W_1. Because the partial cycle 1-2-3 can be represented as the conversion of mechanical energy to electrical energy, the area W_2 is the internal energy that is returned to the environment in mechanical form. The areas W_1 and W_2 can be found by integrating:

$$W_1 = \frac{1}{2}(s_{33}^E - s_{33}^D)\bar{T}_3^2 \tag{2.69}$$

$$W_2 = \frac{1}{2}s_{33}^D\bar{T}_3^2 \tag{2.70}$$

The square of the electromechanical coupling factor is defined as the ratio of energy converted to electrical form (W_1) to the total mechanical energy applied to the specimen ($W_1 + W_2$). Therefore, the coupling factor k_{33} can be derived as in Equation 2.71 below. While the square of the coupling coefficient is useful for comparing the energy conversion ratio of a piezoelectric material, most published material data uses the square root value given previously in Equation 2.63.

$$k_{33}^2 = \frac{W_1}{W_1 + W_2} = \frac{s_{33}^E - s_{33}^D}{s_{33}^E} = \frac{d_{33}^2}{s_{33}^E\varepsilon_{33}^T} \tag{2.71}$$

2. Converse Piezoelectric Effect

The coupling factor is also well defined for conversion from electrical energy to mechanical energy. Consider the same block of piezoelectric material from Fig. 4. This time, an electric field $\bar{E}_3$ is incrementally applied to the material while the specimen is free to expand ($T_3 = 0$). This causes the transition from Point 1 to Point 2 on the $D - E$ diagram in Fig. 6.

Because $T_3 = 0$, the constitutive relations for the transition from Point 1 to Point

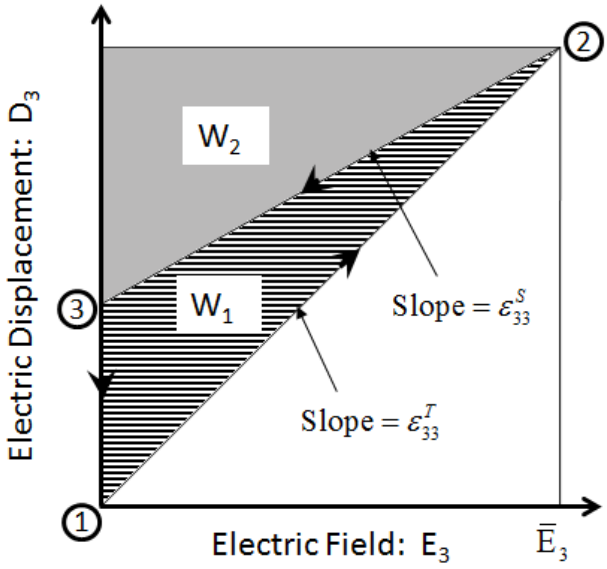

Fig. 6. Graphical interpretation of the electrical to mechanical cycle for the coupling factor k_{33}.

2 reduce to

$$S_3 = d_{33}E_3$$
$$D_3 = \varepsilon_{33}^{T}E_3. \tag{2.72}$$

From Equation 2.72, it is clear that the line representing the transition has a slope of ε_{33}^{T} which is the stress free electric permittivity. The total electrical energy density applied to the specimen is proportional to the area W_1+W_2. When the electric field reaches $\bar{E}_3$ at Point 2 the mechanical boundary condition in the 3 direction is changed to clamped (zero displacement in 3-direction). This causes the strain in the specimen to remain constant at the value $\hat{S}_3$ given in Equation 2.73.

$$\hat{S}_3 = d_{33}\bar{E}_3 \tag{2.73}$$

The electric field is now incrementally reduced to its initial value (Points 2-3) while the specimen remains clamped. The constitutive relations for the transition are given in Equation 2.74. Note that the strain $\hat{S}_3$ remains constant during this part of the cycle.

$$\begin{aligned} \hat{S}_3 &= s_{33}^E T_3 + d_{33} E_3 \\ D_3 &= d_{33} T_3 + \varepsilon_{33}^T E_3 \end{aligned} \tag{2.74}$$

From the first part of the constitutive relation, we know T_3:

$$T_3 = \frac{\hat{S}_3 - d_{33} E_3}{s_{33}^E}. \tag{2.75}$$

Substituting T_3 back into the second part of the constitutive relation, we get:

$$\begin{aligned} D_3 &= d_{33} \left(\frac{\hat{S}_3 - d_{33} E_3}{s_{33}^E} \right) + \varepsilon_{33}^T E_3 \\ &= d_{33} \frac{\hat{S}_3}{s_{33}^E} + \left(\varepsilon^T - \frac{d_{33}^2}{s_{33}^E} \right) E_3 \\ &= d_{33} \frac{\hat{S}_3}{s_{33}^E} + \varepsilon^S E_3. \end{aligned} \tag{2.76}$$

From Equation 2.76, it is clear that the line between Points 2 and 3 has a slope equal to ε_{33}^S, the strain free electric permittivity. Also note that the constant $d_{33} \frac{\hat{S}_3}{s_{33}^E}$ term indicates that the line does not pass through the origin in Fig. 6. This transition reduces the mechanical energy density in the specimen to the area W_1.

At Point 3 there is a residual electric displacement in the material, so an ideal mechanical load is connected which decreases the electric displacement to its initial value at Point 1 which completes the full cycle. The work done on the ideal mechanical load is represented by the area W_1. Because the partial cycle 1-2-3 can be represented as the conversion of electrical energy to mechanical energy, the area W_2 is the internal

energy that is returned to the environment in electrical form. The areas W_1 and W_2 can be found by integrating:

$$W_1 = \frac{1}{2}(\varepsilon_{33}^T - \varepsilon_{33}^S)\bar{E}_3^2 \tag{2.77}$$

$$W_2 = \frac{1}{2}\varepsilon_{33}^S \bar{E}_3^2 \tag{2.78}$$

As in the direct piezoelectric case, the square of the coupling factor can be defined as the ratio of the energy converted to mechanical form (W_1) to the total electrical energy applied to the specimen ($W_1 + W_2$). Hence the coupling factor can be derived using Equation 2.79.

$$k_{33}^2 = \frac{W_1}{W_1 + W_2} = \frac{\varepsilon_{33}^T - \varepsilon_{33}^S}{\varepsilon_{33}^T} = \frac{d_{33}^2}{s_{33}^E \varepsilon_{33}^T} \tag{2.79}$$

In both the direct and converse derivations of k_{33}, the square of the coupling factor was defined as the ratio of energy converted to total energy applied. Because of this, the k_{33}^2 can be viewed as an efficiency of energy conversion. Indeed, the limits of k_{33}^2 must be zero and one which correspond to zero energy conversion and total energy conversion, respectively. A k_{33}^2 value greater than one implies there is more energy converted than energy applied to the material, which is thermodynamically impossible. Actually, even a k_{33}^2 of one is technically impossible because the second law of thermodynamics states that energy conversion with 100% efficiency is impossible.

3. Complex Coupling Factor

The definition of the electromechanical coupling factor can be extended to harmonic analysis using complex material constants. If any of the material constants in Equation 2.79 are complex, the coupling factor k_{33} must therefore be complex. The same convention used to distinguish between the real and imaginary parts of the material

constants can be used with k_{33}.

$$k_{33} = k'_{33} + k''_{33} \tag{2.80}$$

However, for this representation to be of any use, some kind of physical meaning must be associated with the real and imaginary parts of the coupling factor. The following derivation is from [21]. To begin, the instantaneous energy density is defined as

$$w(t) = D(t)E(t) = S(t)T(t). \tag{2.81}$$

Now, consider the same piezoelectric block of material from the static coupling factor definition. A harmonic stress $T = T_0 e^{j\omega t}$ is applied to the material in the 3-direction, and the electrical contacts are shorted. The resulting strain in the 3-direction can be represented by

$$S_3(t) = |s_{33}^E| T_0 e^{j\phi^E} e^{j\omega t}, \tag{2.82}$$

where ϕ^E is the phase lag between the applied stress and resultant strain.

From Equation 2.81, it is easy to see that the total energy density $w_T(t)$ applied to the specimen is

$$w_T(t) = |s_{33}^E| T_0^2 e^{j\phi^E} e^{2j\omega t}. \tag{2.83}$$

The energy density converted to electrical form $w_1(t)$ is simply the difference between the total energy density applied $w_T(t)$ minus the open circuit compliance energy density.

$$w_1(t) = |s_{33}^E| T_0^2 e^{j\phi^E} e^{2j\omega t} - |s_{33}^D| T_0^2 e^{j\phi^D} e^{2j\omega t} \tag{2.84}$$

As was seen in the static coupling factor derivation, the square of the coupling factor is equal to the ratio of energy density converted to electrical form $w_1(t)$ to the

total applied energy density:

$$k_{33}^2 = \frac{w_1(t)}{w_T(t)} = \frac{|s_{33}^E|T_0^2 e^{j\phi^E} e^{2j\omega t} - |s_{33}^D|T_0^2 e^{j\phi^D} e^{2j\omega t}}{|s_{33}^E|T_0^2 e^{j\phi^E} e^{2j\omega t}} \tag{2.85}$$

Simplifying, we get:

$$k_{33}^2 = \frac{|s_{33}^E|T_0^2 e^{j\phi^E} - |s_{33}^D|T_0^2 e^{j\phi^D}}{|s_{33}^E|T_0^2 e^{j\phi^E}} = \frac{s_{33}^E - s_{33}^D}{s_{33}^E} = \frac{d_{33}^2}{s_{33}^E \varepsilon_{33}^T}, \tag{2.86}$$

where s_{33}^E, s_{33}^D, d_{33}, and ε_{33}^T are complex numbers.

The complex coupling factor can also be derived from the converse effect. Consider the same piezoelectric material specimen. A harmonic electric field $E = E_0 e^{j\omega t}$ is applied to the material in the 3-direction, and the specimen is free to expand. The resulting electric displacement in the 3-direction is given by

$$D_3(t) = |\varepsilon_{33}^T| E_0 e^{j\phi^T} e^{j\omega t}. \tag{2.87}$$

From Equation 2.81, it is easy to see that the total energy density $w_T(t)$ applied to the specimen is

$$w_T(t) = |\varepsilon_{33}^T| E_0^2 e^{j\phi^T} e^{2j\omega t}. \tag{2.88}$$

The energy density converted to electrical form $w_1(t)$ is simply the difference between the total energy density applied $w_T(t)$ minus the open circuit compliance energy density.

$$w_1(t) = |\varepsilon_{33}^T| E_0^2 e^{j\phi^T} e^{2j\omega t} - |\varepsilon_{33}^S| E_0^2 e^{j\phi^S} e^{2j\omega t} \tag{2.89}$$

As was seen in the static coupling factor derivation, the square of the coupling factor is equal to the ratio of energy density converted to electrical form $w_1(t)$ to the total applied energy density:

$$k_{33}^2 = \frac{w_1(t)}{w_T(t)} = \frac{|\varepsilon_{33}^T| E_0^2 e^{j\phi^T} e^{2j\omega t} - |\varepsilon_{33}^S| E_0^2 e^{j\phi^S} e^{2j\omega t}}{|\varepsilon_{33}^T| E_0^2 e^{j\phi^T} e^{2j\omega t}} \tag{2.90}$$

Simplifying, we get:

$$k_{33}^2 = \frac{|\varepsilon_{33}^T|E_0^2 e^{j\phi^T} - |\varepsilon_{33}^S|E_0^2 e^{j\phi^S}}{|\varepsilon_{33}^T|E_0^2 e^{j\phi^T}} = \frac{\varepsilon_{33}^T - \varepsilon_{33}^S}{\varepsilon_{33}^T} = \frac{d_{33}^2}{s_{33}^E \varepsilon_{33}^T}, \tag{2.91}$$

where ε_{33}^T, ε_{33}^S, d_{33}, and s_{33}^E are complex numbers. The real and imaginary parts of k_{33}^2 can be physically interpreted in the same way that complex permittivity was. The real part is a measure of the conversion efficiency between the electrical and mechanical energy densities. The imaginary part is a measure of the phase lag between the energy densities.

It should be noted that there has recently been put forth an alternative to the preceding derivation of a complex valued coupling factor. According to Piquette and McLaughlin [34], the derivation by Lamberti et al. [21] is mathematically flawed. Specifically, they argue that Equation 2.90 is not correct because it assumes real and imaginary parts for each term, and they contend that this is not consistent with the definitions of instantaneous energy density. To overcome this issue, they derived the coupling factor from fundamental fields and stresses using energy densities averaged over a single drive cycle. The result for the coupling factor k_{33} is given as:

$$k_{33}^2 = \frac{(d'_{33})^2}{\varepsilon_{33}^{T'} s_{33}^{E'}} \tag{2.92}$$

Surprisingly, this is the same result as Equation 2.91 except that only the real values of the material properties are used. However, there is an important requirement for this equation to hold. Namely, the applied harmonic stress and harmonic electric fields must be in phase, or the coupling factor obtained from this definition will not be independent of the applied fields and stresses. Not surprisingly, this definition of the coupling factor produces results that are quite different from those produced by the definition from Lamberti et al. Because most of this work had been completed before [34] was published, the decision was made not to use the new definition in this

work. However, future work should definitely attempt to determine the usefulness and correctness of the new definition.

CHAPTER III

COMPUTATIONAL MODELS

A. Configurations

Two basic configurations were considered in this work. The first is a cubic representative volume element (RVE) as shown in Fig. 7. The second configuration is a hexagonal prism RVE as shown in Fig. 8. Each RVE consists of a spherical PZT inclusion imbedded in a polymer matrix. Piezoelectric material properties were used for the PZT inclusion, and the polymer matrix was modeled with uncoupled electrical and mechanical responses. For both configurations, the material axes for the PZT inclusions were assumed to be perfectly aligned with the global coordinate system.

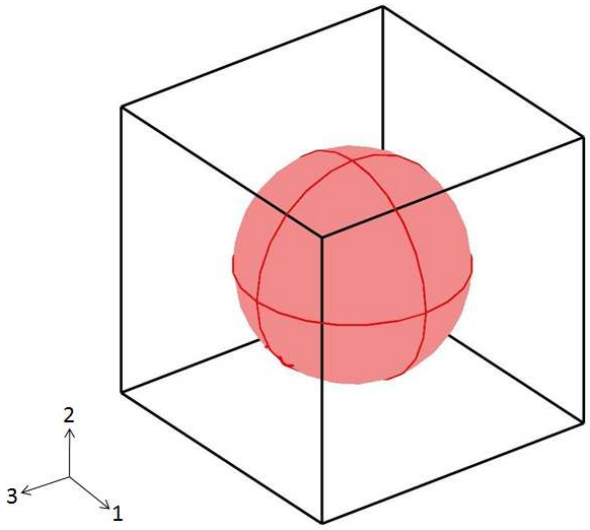

Fig. 7. Cubic RVE.

It should be noted that with periodic boundary conditions applied in all directions, the cubic RVE represents a three dimensional cubic array of PZT particles.

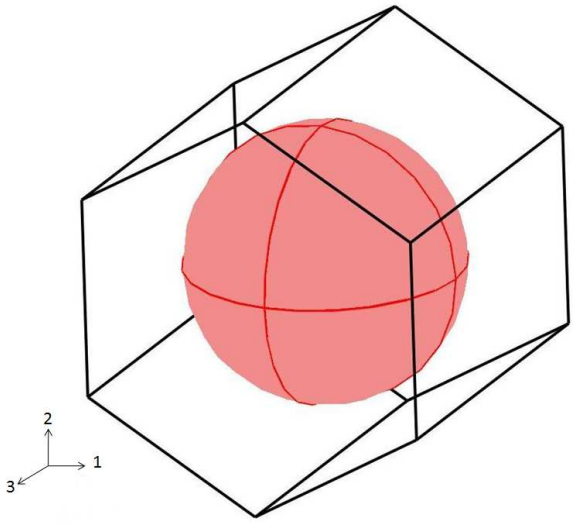

Fig. 8. Hexagonal RVE.

However, the hexagonal RVE represents a hexagonal packed array of particles in the 1- and 2- material directions and a cubic array in the 3- material direction, which can be seen in Fig. 9.

B. Periodic Boundary Conditions

Exact periodic boundary conditions (PBCs) were applied to the FEA models using formulations given in Whitcomb et al. [35]. The PBCs relate displacements, stresses, electric potential, and electric displacement between opposing boundaries of RVE. Volume averaged strains and electric potentials can be applied through the PBCs.

The displacement and traction periodic boundary conditions are given in Equation 3.1 where u_i is the displacement vector, x_α is the position vector, T_{ij} is the stress tensor, and d_β is the vector of periodicity. Mechanical loads are applied to the model as volume averaged displacement gradients.

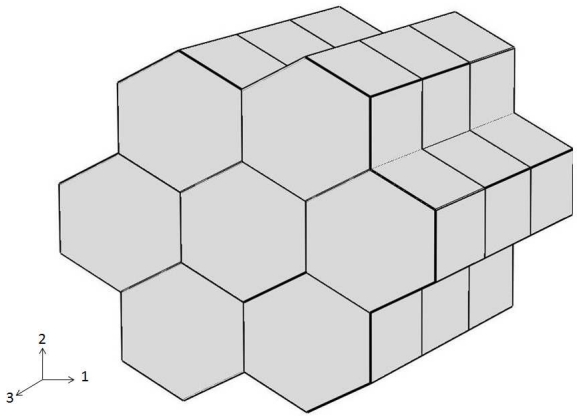

Fig. 9. Array of hexagonal RVEs with hexagonal packing in 1- and 2-directions and square packing in the 3-direction.

$$u_i(x_\alpha + d_\alpha) = u_i(x_\alpha) + \left\langle \frac{\partial u_i}{\partial x_\beta} \right\rangle d_\beta$$
$$T_{ij}(x_\alpha + d_\alpha) = T_{ij}(x_\alpha) \tag{3.1}$$

The electrostatic boundary conditions are given in Equation 3.2 where V is electric potential (voltage) and D_i is the electric displacement vector. Electric loads are applied as volume averaged potential gradients.

$$V(x_\alpha + d_\alpha) = V(x_\alpha) + \left\langle \frac{\partial V}{\partial x_\beta} \right\rangle d_\beta$$
$$D_i(x_\alpha + d_\alpha) = D_i(x_\alpha) \tag{3.2}$$

The periodic boundary conditions were verified by creating a large array of RVEs and applying the periodic boundary conditions to the outer boundaries of the array. The resulting stress, strain, electric displacement, and electric fields were checked to verify that they were identical in each RVE. Since the periodic PBCs were only

applied to the outer RVEs, identical electrical and mechanical fields in each RVE indicate that the PBCs were exactly satisfied.

C. Material Properties

The three-phase piezoelectric nanocomposite studied is based on nanocomposites made by Ounaies et al. [4]. It consists of a βCN-PI matrix with single wall nanotube (SWNT) and piezoelectric PZT-5A particle inclusions. A two-phase piezoelectric nanocomposite was also modeled in order to compare results to results from the literature. The material system consists of a LaRC-SI matrix and PZT-7A particle inclusions. Again note that for both material systems considered, the material directions of the PZT particles were assumed to be perfectly aligned with the global coordinate system.

The properties for all materials used in this work are given in Table I. The material properties for βCN-PI/SWNT were taken from the experimental results in [5]. The electrical permittivity values are shown in Fig. 10. An exponential fit was used to interpolate permittivities in between the experimental values, and this is shown in the figure as well. The experimental permittivities for the three-phase βCN-PI/SWNT/PZT specimens, also from [5], are given in Fig. 11. Since only three data points were available, a quadratic polynomial (given in the figure) was used to interpolate values in between these three points when needed. All of the permittivity values used in this work are normalized by the permittivity of free space, $\varepsilon_0 = 8.854 \times 10^{-12} F/m$. It should be stressed at this point that the volume fractions of nanotubes given in Fig. 11 correspond to the fraction of nanotubes in the entire three-phase composite. However, whenever FEA results are given in this work, the volume fraction correpsonds to the fraction of nanotubes in the βCN-PI/SWNT matrix.

Table I. Material properties.

	LaRC-SI	PZT-7A	βCN-PI	βCN-PI/ 0.1% SWNT	βCN-PI/ 0.2% SWNT	PZT-5A	Unpoled PZT-5A
c_{11}^E (GPa)	8.1	148	5.32	5.5	5.69	120.3	88.0
c_{12}^E (GPa)	5.4	76.2	3.47	3.57	3.65	75.2	37.7
c_{13}^E (GPa)	5.4	74.2	3.47	3.57	3.65	75.1	37.7
c_{22}^E (GPa)	8.1	148	5.32	5.5	5.69	120.3	88.0
c_{23}^E (GPa)	5.4	74.2	3.47	3.57	3.65	75.1	37.7
c_{33}^E (GPa)	8.1	131	5.32	5.5	5.69	110.9	88.0
c_{44}^E (GPa)	1.4	25.4	0.922	0.969	1.02	21.1	25.1
c_{55}^E (GPa)	1.4	25.4	0.922	0.969	1.02	21.1	25.1
c_{66}^E (GPa)	1.4	35.9	0.922	0.969	1.02	22.6	25.1
$\varepsilon_{11}^S/\varepsilon_0$	2.8	460	3.75	36.5	346	919	1000
$\varepsilon_{22}^S/\varepsilon_0$	2.8	460	3.75	36.5	346	919	1000
$\varepsilon_{33}^S/\varepsilon_0$	2.8	235	3.75	36.5	346	827	1000
$e_{15}(C/m^2)$	0	9.2	0	0	0	12.3	0
$e_{31}(C/m^2)$	0	-2.1	0	0	0	-5.35	0
$e_{32}(C/m^2)$	0	-2.1	0	0	0	-5.35	0
$e_{33}(C/m^2)$	0	9.5	0	0	0	15.78	0

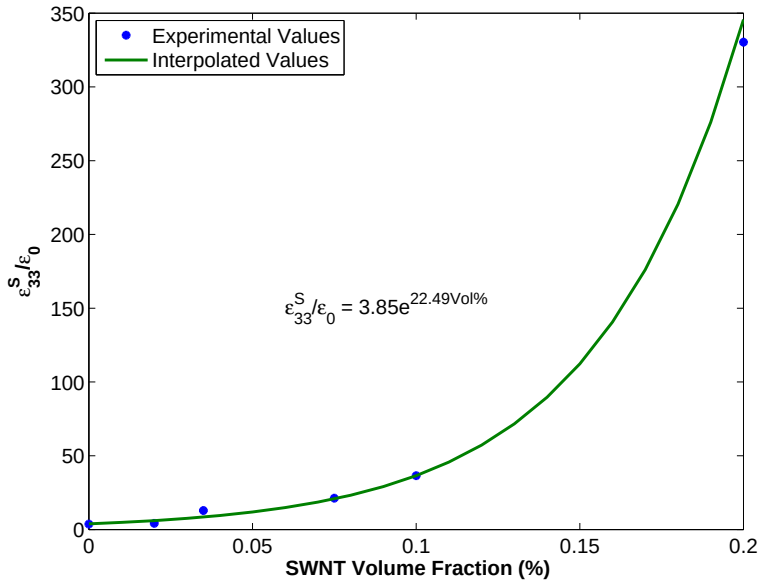

Fig. 10. Experimental permittivity of βCN-PI/SWNT as a function of SWNT volume fraction (%).

D. Calculation of Effective Material Properties

In order to calculate all of the effective piezoelectric material properties, a series of nine different load cases were applied to the model. The load cases consisted of three uniaxial strains, three shear strains, and three electric fields as shown in Table II. Each load case allowed the calculation of one or more material constants. The effective coefficients calculated at each load step are given in Table III.

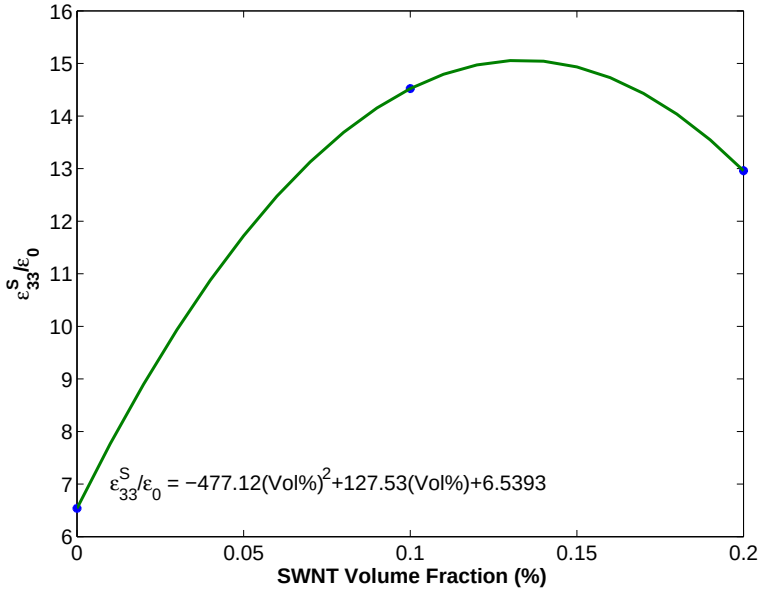

Fig. 11. Experimental permittivity of three-phase βCN-PI/SWNT/PZT as a function of SWNT volume fraction (%).

Table II. Summary of load cases used to calculate all effective properties.

Load Case	$\frac{\partial u_1}{\partial x_1}$	$\frac{\partial u_2}{\partial x_2}$	$\frac{\partial u_3}{\partial x_3}$	$\frac{\partial u_2}{\partial x_1}$	$\frac{\partial u_3}{\partial x_1}$	$\frac{\partial u_1}{\partial x_2}$	$\frac{\partial u_3}{\partial x_2}$	$\frac{\partial u_1}{\partial x_3}$	$\frac{\partial u_2}{\partial x_3}$	$\frac{\partial V}{\partial x_1}$	$\frac{\partial V}{\partial x_2}$	$\frac{\partial V}{\partial x_3}$
1	0.001	0	0	0	0	0	0	0	0	0	0	0
2	0	0.001	0	0	0	0	0	0	0	0	0	0
3	0	0	0.001	0	0	0	0	0	0	0	0	0
4	0	0	0	0	0	0	0.001	0	0.001	0	0	0
5	0	0	0	0	0.001	0	0	0.001	0	0	0	0
6	0	0	0	0.001	0	0.001	0	0	0	0	0	0
7	0	0	0	0	0	0	0	0	0	10	0	0
8	0	0	0	0	0	0	0	0	0	0	10	0
9	0	0	0	0	0	0	0	0	0	0	0	10

Table III. Effective coefficients calculated for each load case.

Load Case	Effective Coefficient(s) Calculated
1	$c_{11}, c_{12}, c_{13}, e_{31}$
2	c_{22}, c_{23}
3	c_{33}, e_{33}
4	c_{44}
5	c_{55}
6	c_{66}
7	ε_{11}, e_{24}
8	ε_{22}, e_{15}
9	ε_{33}

CHAPTER IV

RESULTS AND DISCUSSION

A. Comparison to Results from Literature

A special FEA model was developed to compare predicted effective properties with results from [23]. The hexagonal RVE and LaRC-SI/PZT-7A material properties used match the finite element analysis performed by Odegard. It must be stressed, however, that Odegard used multiple RVE's connected together to form a larger finite element model. Displacement and traction boundary conditions were applied to the outer surfaces of the full model, and the properties were predicted at the innermost RVE. The boundary conditions used represented approximate periodic boundary conditions. As the number of RVEs in the array increases, the solution at the innermost RVE approaches the exact periodic solution. The hexagonal model in this work used exact periodic boundary conditions applied to the boundaries of a single RVE.

In addition to a finite element analysis, Odegard also predicted effective piezoelectric properties using several micromechanics models. These included self consistent and Mori-Tanaka schemes as well as a novel, proposed scheme. In this work Odegard's FEA and micromechanics predictions were used for comparison.

The effective permittivity $\varepsilon_{11}^{S}/\varepsilon_0$ is shown in Fig. 12 as a function of PZT volume fraction. Overall, the trends are the same for each of the methods shown. The permittivity increases with PZT volume fraction which is expected because the permittivity of the PZT is so much higher than the LaRC-SI matrix. Also, the various methods show better agreement at lower volume fractions.

The effective piezoelectric coefficient e_{31} is shown in Fig. 13. There is much more variation between the different methods for e_{31} than there was for the permittivity.

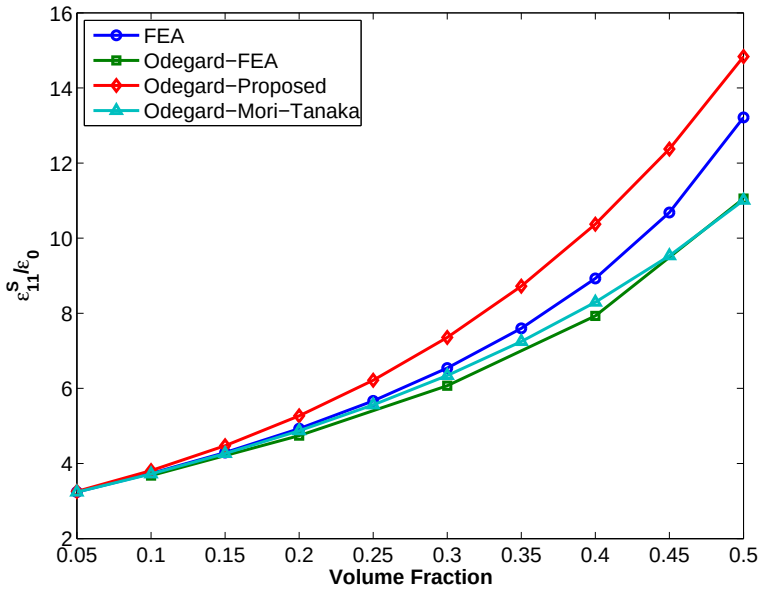

Fig. 12. Effective $\varepsilon_{11}^S/\varepsilon_0$ as a function of PZT volume fraction.

An interesting result of the comparison is that Odegard's FEA predictions do not seem to match the micromechanics models very well, even at low volume fractions. This is most likely due to the use of approximate periodic boundary conditions in his FEA model.

The effective piezoelectric coefficient e_{33} is given in Fig. 14. There is again a noticeable amount of variation between the predictions, especially at higher volume fractions. Also, Odegard's FEA results due not agree as well throughout the entire range of PZT volume fraction. This is again attributed to the use of approximate boundary conditions.

While the comparison of FEA predictions to Odegard's work does not completely validate the model being used, it still shows that the FEA model does give reasonable results over a wide range of inclusion volume fraction. The comparison also highlights the fact that exact periodic boundary conditions are extremely important if accurate

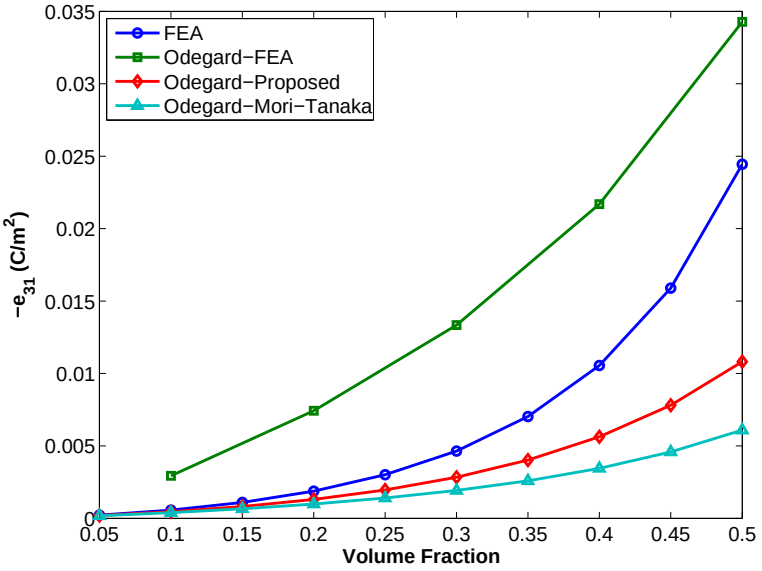

Fig. 13. Effective $-e_{31}$ as a function of PZT volume fraction.

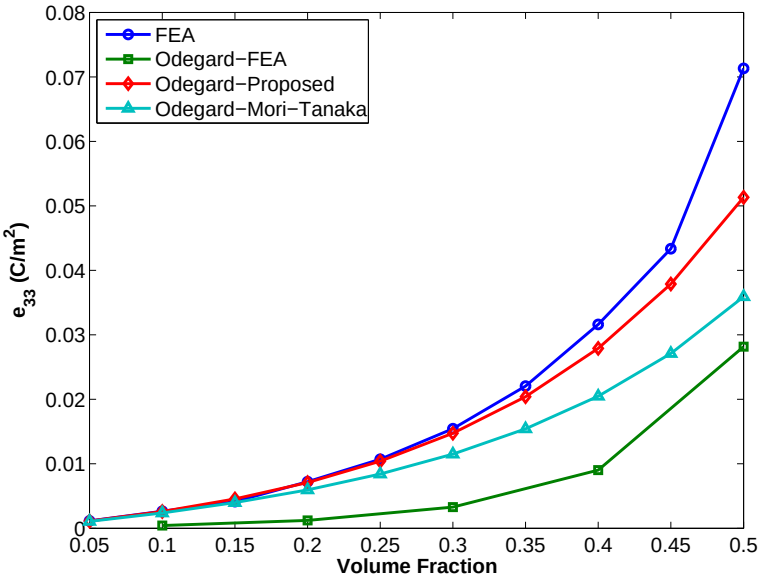

Fig. 14. Effective e_{33} as a function of PZT volume fraction.

predictions are desired.

There were also several comparisons made to experimental results in the literature. Three different sets of experimental results for PZT/PVDF piezoelectric composites were taken from Poon et al. [36], and the constituent properties in that work were used in a finite element model with a cubic RVE. The piezoelectric coefficients d_{33} or d_{31} were predicted and compared to the experimental results. It should be noted that Poon et al. only presented the experimental data from other sources for comparison to their analytical model. The experimental data was taken from their work by digitizing the appropriate figures.

The first set of data was from Chan et al. [37] and their experimental results for d_{33} are plotted along with the predictions from the FEA model in Fig. 15. The second set of data was from Furukawa [38], and the experimental results for d_{31} are given alongside the FEA predictions in Fig. 16. The final set of experimental results from Venkatragavaraj et al. [39] are compared to FEA predictions in Fig. 17.

The comparisons to experiment show that the finite element model can predict piezoelectric performance reasonably well for smaller volume fractions of PZT. However, at volume fractions around 50%, the FEA and experimental results do not agree nearly as well. This is due to the fact that the finite element model assumes a perfect cubic array of perfectly spherical PZT particles. At lower volume fractions, this is a reasonable approximation of the actual microstructure, but at higher volume fractions, the differences between the actual and assumed microstructure contribute more to the difference in predicted properties. In future work, a more realistic RVE with randomly spaced and sized PZT particles could be used to get better results at higher volume fractions. It should also be noted that the piezoelectric coefficients for PZT/PVDF composites from experiment and FEA are lower than the coefficients for PVDF alone. This is a direct result of the dielectric mismatch between the ceramic

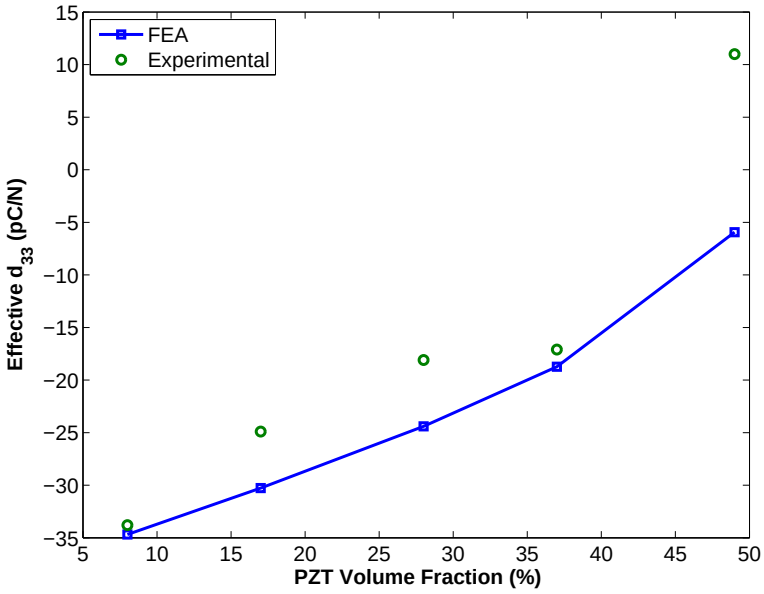

Fig. 15. Effective d_{33} as a function of PZT volume fraction.

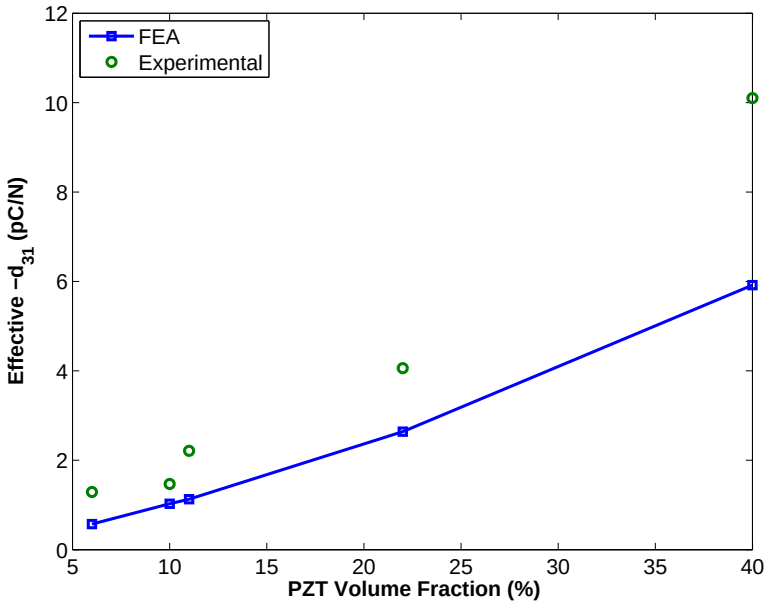

Fig. 16. Effective $-d_{31}$ as a function of PZT volume fraction.

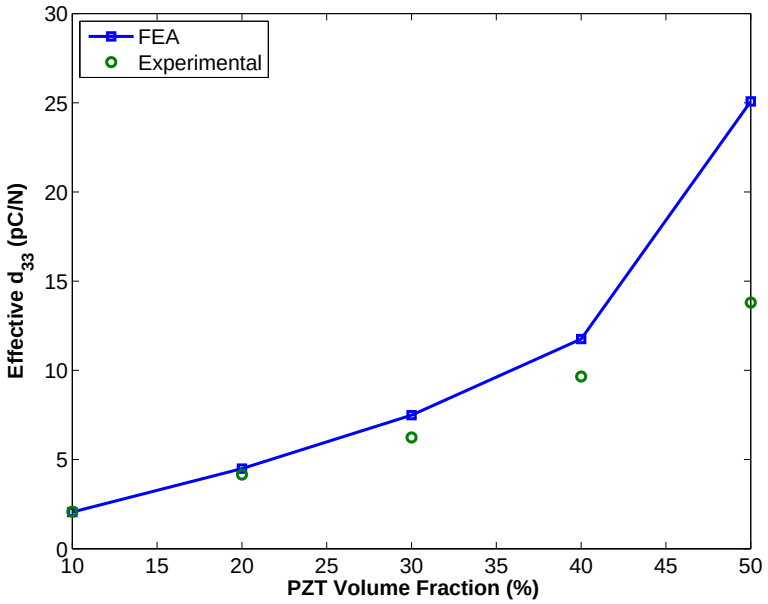

Fig. 17. Effective d_{33} as a function of PZT volume fraction.

and polymer and highlights the need for carbon nanotubes in order to achieve better piezoelectric peformance.

B. Parametric Studies Under Static Conditions

1. Volume Fraction Effects

A parametric study was performed to predict properties of the three-phase nanocomposite under static conditions. The effective properties were obtained for various concentrations of PZT and nanotubes. The effective permittivity $\varepsilon_{11}^S/\varepsilon_0$ is shown in Fig. 18 as a function of the volume fraction of nanotubes for different concentrations of PZT. It is clear that the permittivity increases with both increasing nanotube and PZT content. The effective permittivity $\varepsilon_{33}^S/\varepsilon_0$ is shown in Fig. 19. The trend is very similar to that in Fig. 18, but the $\varepsilon_{11}^S/\varepsilon_0$ values are higher.

The effective permittivity $\varepsilon_{33}^S/\varepsilon_0$ for 20% PZT is shown again in Fig. 20. The

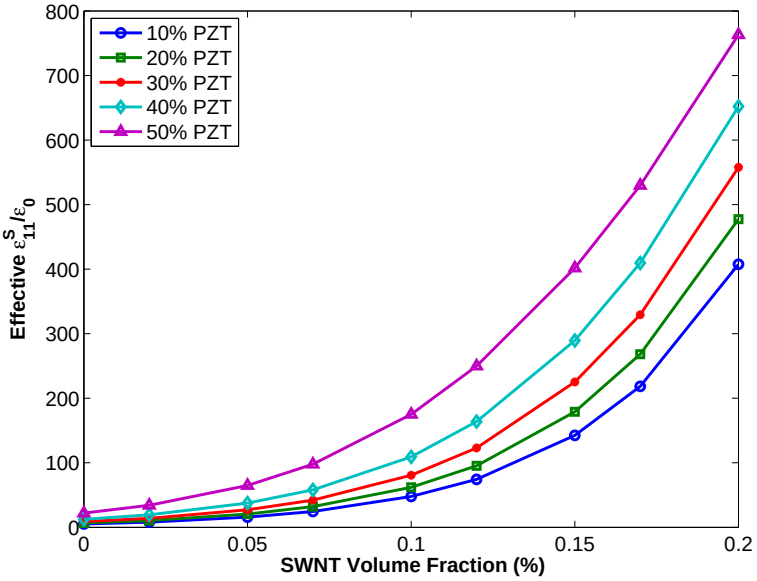

Fig. 18. Effective $\varepsilon^S_{11}/\varepsilon_0$ as a function of SWNT volume fraction (%).

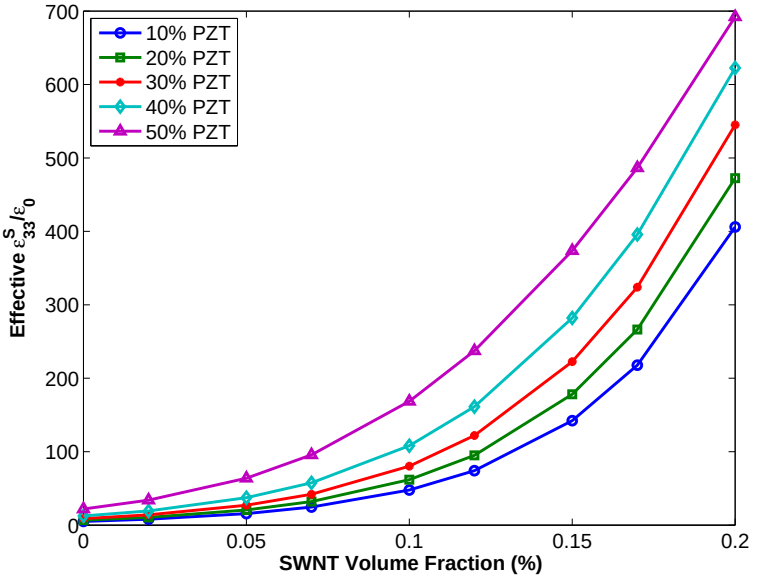

Fig. 19. Effective $\varepsilon^S_{33}/\varepsilon_0$ as a function of SWNT volume fraction (%).

experimental values for this PZT concentration is also given for several SWNT concentrations. It is seen in the figure that the predicted permittivities are much higher than the experimental values. This indicates that there is some phenomenon that is not being modeled in the finite element model. This could include quantum effects like electron tunneling, an assumed microstructure that does not represent the actual microstructure, or simply inaccurately assumed constituent properties. Again, note that the volume fractions for the experimental values correspond to the fraction of nanotubes in the entire three-phase composite whereas the FEA volume fractions correspond to the fraction of nanotubes in the βCN-PI/SWNT matrix. The difference between the two volume fractions is assumed to be small enough that a direct comparison between FEA and experiment can be made.

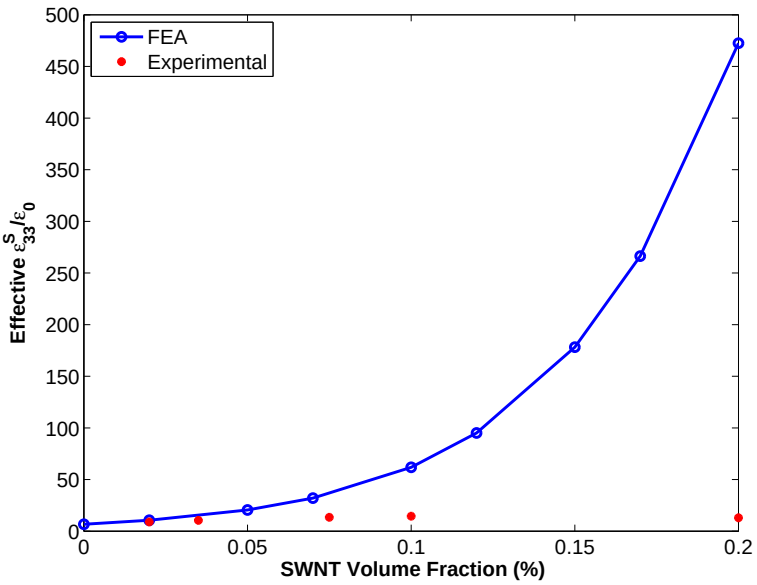

Fig. 20. Effective $\varepsilon_{33}^S/\varepsilon_0$ as a function of SWNT volume fraction (%).

The piezoelectric coefficient e_{33} is shown in Fig. 21 as a function of nanotube

volume fraction for different concentrations of PZT. As in the case of the permittivities, the piezoelectric coefficient increases with increasing concentrations of nanotubes and PZT. However, the difference between the 10% PZT and the 50% PZT is much greater for e_{33}. The piezoelectric coefficient e_{31} is given in Fig. 22. Note that the absolute values of the coefficient are given in the plot. The same trends as Fig. 21 are seen. Even though the results show large gains in piezoelectric capabilities, it is important to note that the over-prediction in electric permittivity most likely indicates that the piezoelectric coefficients are over-predicted as well. The results could not be compared to experiment because experimental data was not available for the piezoelectric coefficients.

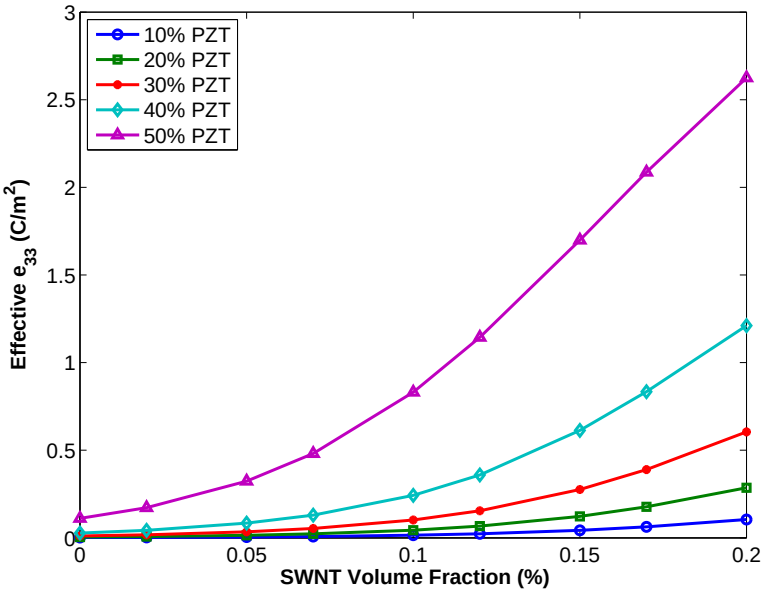

Fig. 21. Effective e_{33} as a function of SWNT volume fraction (%).

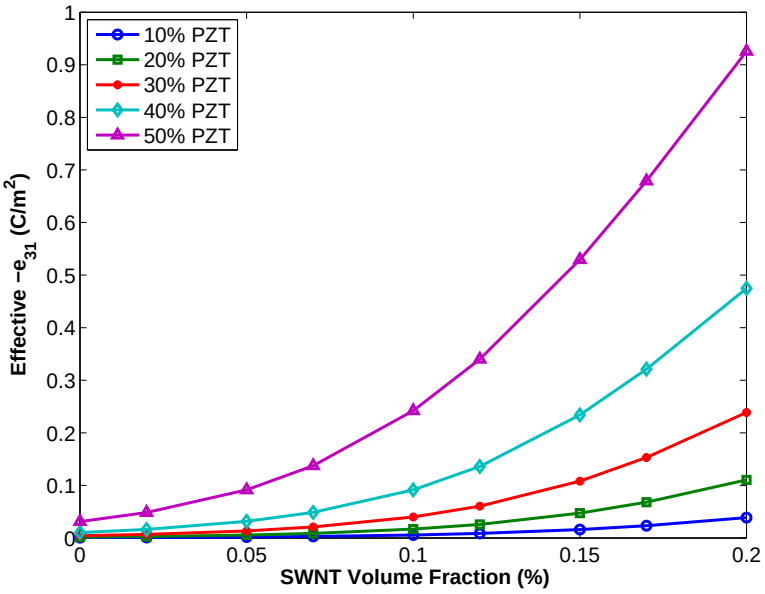

Fig. 22. Effective $-e_{31}$ as a function of SWNT volume fraction (%).

2. Apparent Permittivity of Specimen Matrix

In order to try and explain the discrepancy between FEA and experimental results, a parametric study was performed to find the apparent permittivity of the three-phase specimen matrix. The permittivity of the FEA matrix was varied so that the resulting effective permittivity matched the experimental permittivity. A secant method linear solver was used to quickly find the correct matrix permittivity values. In this way, the exact FEA matrix permittivity needed to match the effective permittivity was found in less than ten iterations. The results are shown in Fig. 23. It is clear from the figure that the apparent permittivities of the in-situ matrix are much less than the experimental values for βCN-PI/SWNT (refer to Fig. 10 for experimental values). This could indicate that there are dispersion issues in the three-phase samples and/or nano-effects that are not being modeled.

The results in Fig. 23 were used to find the effective properties the material

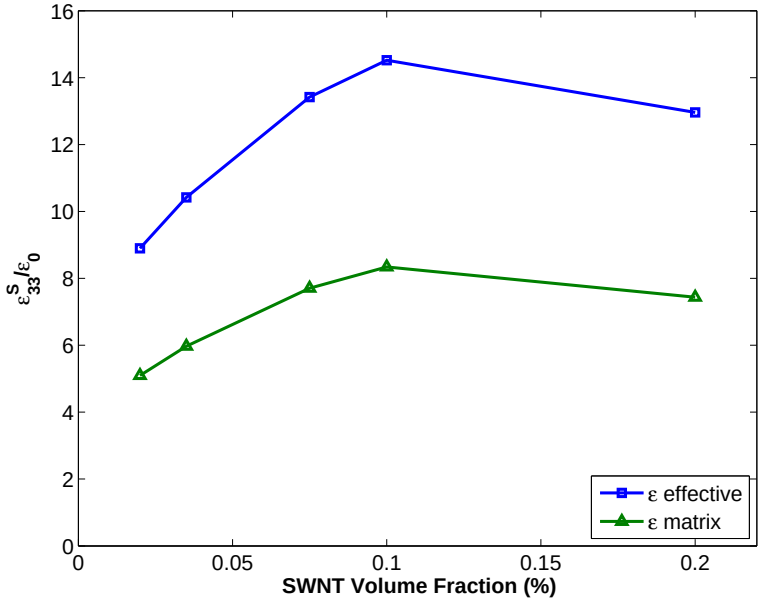

Fig. 23. Apparent matrix permittivity vs. SWNT volume fraction (%).

would have if the matrix permittivities were set to the apparent permittivities. The piezoelectric coefficients e_{31} and e_{33} are given in Fig. 24 as functions of nanotube volume fraction for 20% PZT. It is clear from the results that the piezoelectric response using apparent permittivities is much lower than the response using experimental βCN-PI/SWNT properties.

3. Effect of PZT Poling

Up to this point it has been assumed that the PZT particles in the nanocomposite have been perfectly poled. However, the apparent permittivities of the matrix for the three-phase samples indicate that the PZT may not have been completely poled, and this may explain the discrepancy between FEA and experimental values for permittivity. In order to investigate the effect unpoled PZT particles would have on the effective properties, the material properties for unpoled PZT-5A, given in Paradies

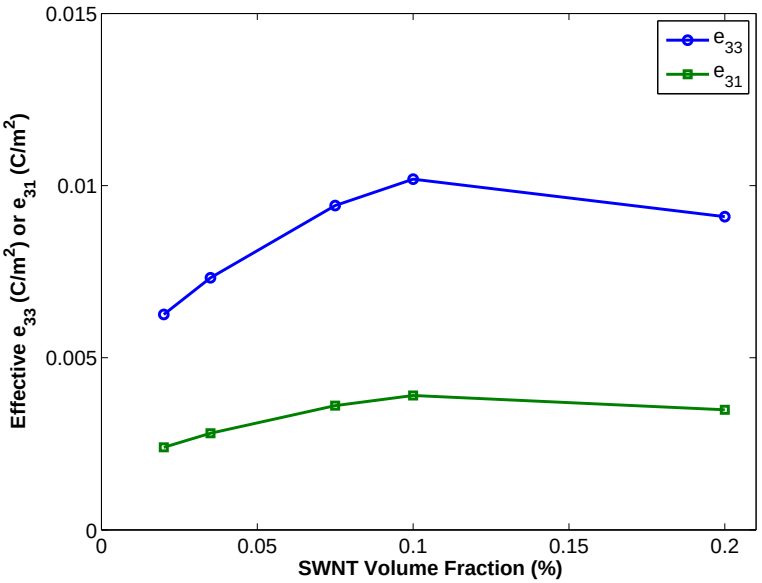

Fig. 24. Piezoelectric coefficients e_{33} or e_{31} vs. SWNT volume fraction (%) for apparent matrix permittivity and 20% PZT.

and Schlapfer [40], were used for the particle inclusions. Refer to Table I for the specific properties used.

Figure 25 gives the variation of $\varepsilon_{33}^{S}/\varepsilon_0$ with respect to SWNT concentration for the cases of poled PZT, unpoled PZT, and experimental values. Even though the permittivities of the unpoled case are less than the poled permittivities, there is still a large difference between the unpoled and experimental results. Therefore, it is reasonable to assume that the discrepancy between the FEA and experimental results is not due solely to partial poling of the PZT.

4. Polymer Interphase Model

Because the FEA permittivities were all much higher than experimental values, a modified model was used to try and match the effective permittivity. A spherical interphase region was added around the PZT inclusion, and the material properties of

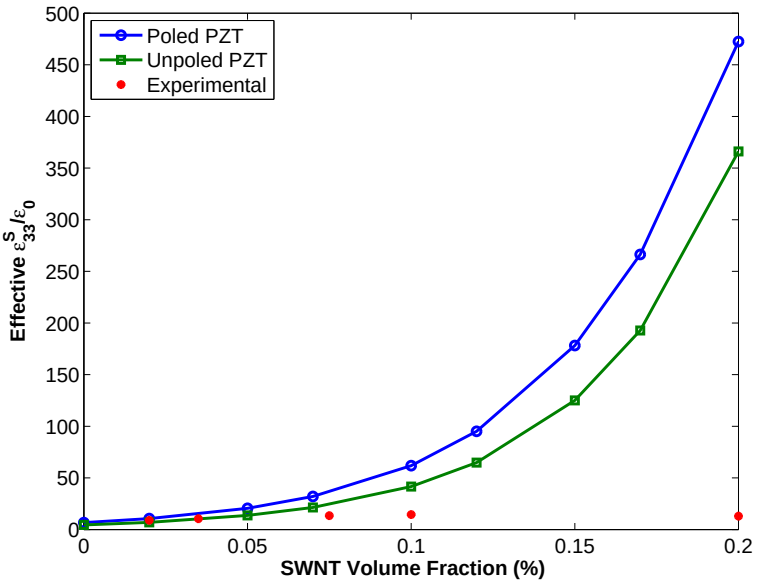

Fig. 25. Comparison of electric permittivity $\varepsilon_{33}^S/\varepsilon_0$ vs. SWNT volume fraction (%) for poled and unpoled PZT.

the interphase were set to the properties of the neat polymer. The interphase volume fraction was then varied to see if it was possible to reproduce experimental effective permittivities with this modified FEA model. A schematic of the interphase model is shown in Fig. 26. The diagram shows the minimum and maximum interphase volume fractions used. The maximum volume fraction of 31.7% corresponds to the largest spherical interphase that could fit inside the cubic RVE. Note that the diagram is a 2D projection of 3D shapes, so apparent volume fractions can be misleading.

The effective permittivity $\varepsilon_{33}^S/\varepsilon_0$ for 0.1% SWNT is given as a function of polymer interphase volume fraction in Fig. 27. The experimental permittivity value for 0.1% SWNT is also given in the figure. It is clear from the results that even the maximum polymer interphase volume fraction cannot match the effective permittivity with the experimental permittivity.

The effective permittivity $\varepsilon_{33}^S/\varepsilon_0$ for 0.2% SWNT is given as a function of polymer

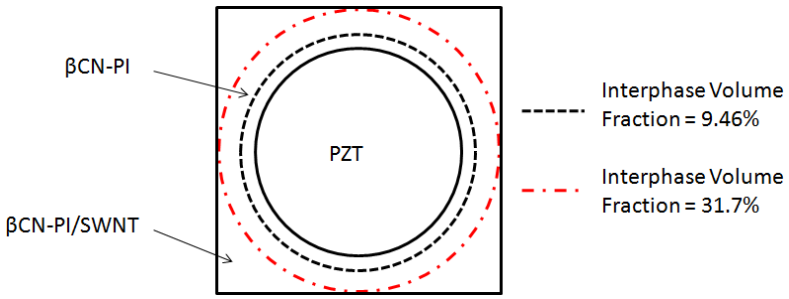

Fig. 26. Diagram of polymer interphase model.

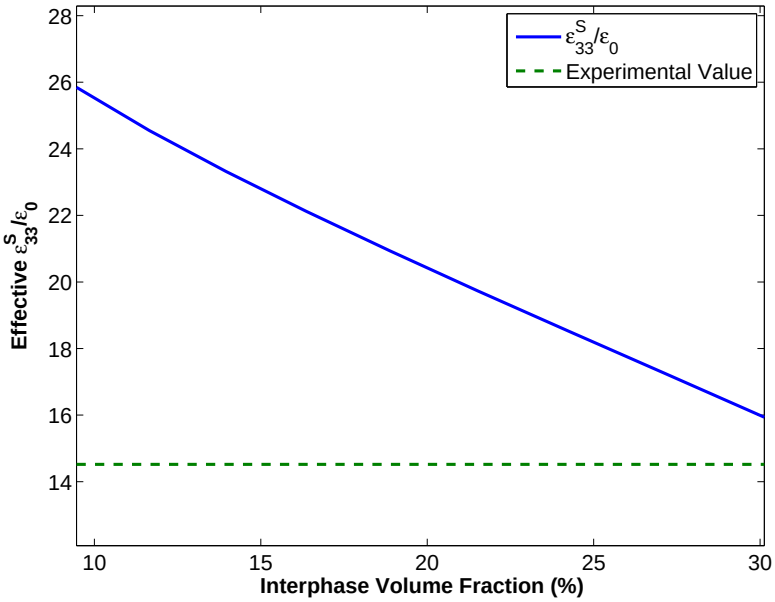

Fig. 27. Effective permittivity vs. polymer interphase volume fraction for 0.1% SWNT.

interphase volume fraction in Fig. 28. The experimental permittivity value for 0.2% SWNT is also given in the figure. Similar to the results for the 0.1% volume fraction, it the polymer interphase cannot match the effective permittivity with the experimental permittivity. Clearly, the polymer interphase model does not capture the material distribution of the three-phase nanocomposite well enough to predict the effective properties accurately.

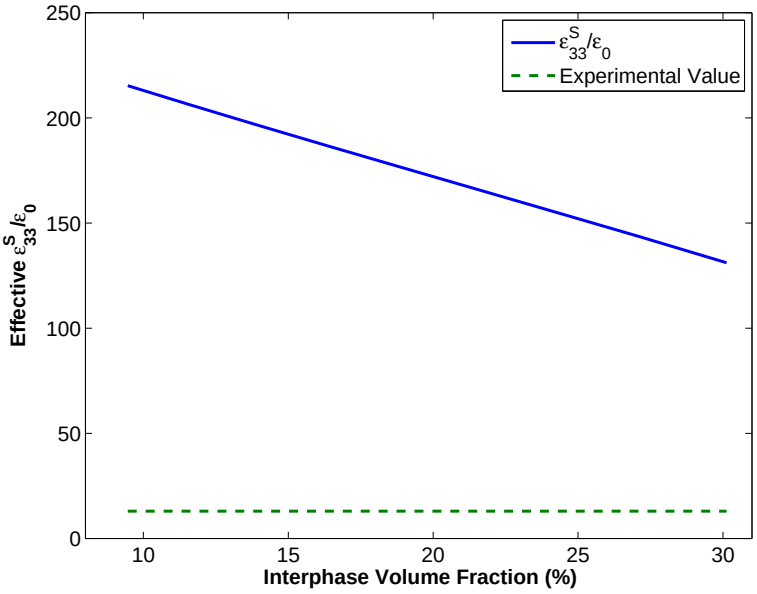

Fig. 28. Effective permittivity vs. polymer interphase volume fraction for 0.2% SWNT.

5. Agglomerated Nanotube Interphase Model

A second interphase model was created to attempt to understand the material distribution of the nanocomposite. In this model, a spherical interphase around the PZT inclusion is assumed to have a high concentration of nanotubes. The matrix material outside the interphase is assumed to have the properties of the neat polymer. This

distribution of material properties represents the phenomenon of nanotube agglomeration around the PZT inclusion. This makes physical sense because dispersion of nanotubes is still a serious issue, as noted in [6, 4]. A schematic of the model is given in Fig. 29. Again, please note that the diagram is a 2D projection of 3D shapes.

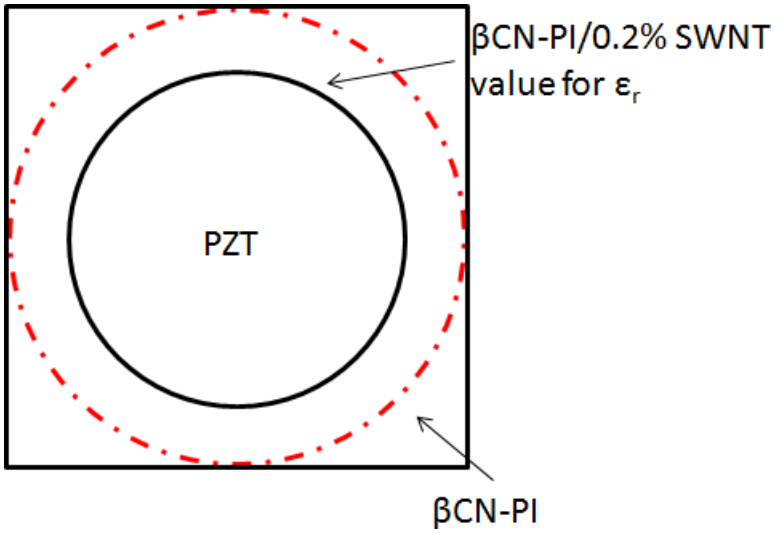

Fig. 29. Diagram of agglomerated nanotube interphase model.

The effective permittivity $\varepsilon_{33}^{S}/\varepsilon_0$ is given as a function of agglomerated interphase volume fraction in Fig. 30. The experimental permittivities for the three-phase composite with 0.1% and 0.2% SWNT are also shown for reference. It is easy to see that the effective permittivity matches the experimental permittivity at approximately 24.5% and 22% interphase volume fraction for the 0.1% and 0.2% SWNT cases, respectively. Because the choice to use the permittivity value for 0.2% SWNT in the interphase was based solely on this value being the highest expermimental permittivity of the βCN-PI/SWNT matrix, another model was run with the interphase permittivity set to the experimental value for 0.1% SWNT. Since the actual concen-

tration of the SWNT in the interphase region is not known, it is reasonable to assume the concentration is somewhere between the 0.1% and 0.2% cases. The results for the 0.1% case are shown in Fig. 31 where the effective permittivity $\varepsilon_{33}^{S}/\varepsilon_0$ is given as a function of agglomerated interphase volume fraction. The figure shows that the lower permittivity interphase can still match the experimental values.

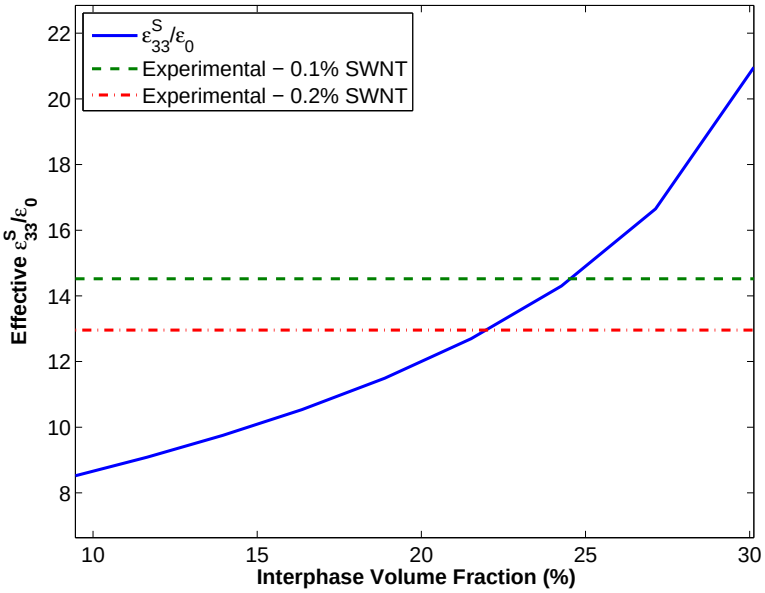

Fig. 30. Effective $\varepsilon_{33}^{S}/\varepsilon_0$ vs. interphase volume fraction (%) for 0.2% SWNT interphase.

Because the effective permittivities of the agglomerated interphase model can be made to match experimental properties, it can be concluded that this model gives a possible material distribution of the three-phase nanocomposite. This material distribution indicates that there are agglomerations of nanotubes around the PZT inclusion and areas with little to no concentrations of nanotubes farther away from the PZT. This distribution is also in agreement with experimental evidence [41] that

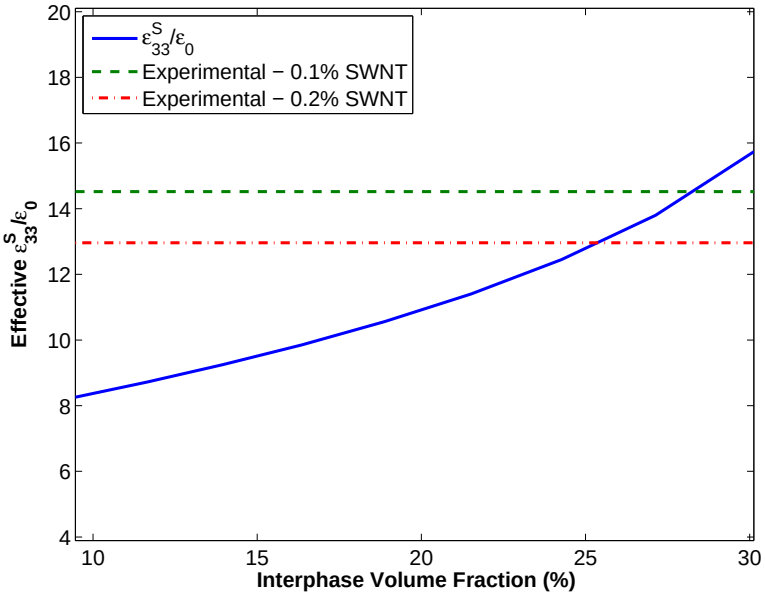

Fig. 31. Effective $\varepsilon_{33}^S/\varepsilon_0$ vs. interphase volume fraction (%) for 0.1% SWNT interphase.

nanotubes form agglomerations easily, and this greatly affects the electrical properties of the composite. If the discrepancy between FEA and experimental permittivities is indeed caused by dispersion issues in the experimental samples, then the parametric studies without interphase can be considered estimations of properties assuming perfect dispersion. It should be stressed that the material distribution used in the agglomerated interphase model is only one possible distribution that the material might have. Indeed, there are an infinite number of material distributions that could give the same effective properties, but the aforementioned experimental evidence showing SWNT agglomerations makes the chosen distribution a reasonable one.

C. Parametric Studies Under Harmonic Loading

A parametric study was performed to predict material properties of the three-phase nanocomposite under harmonic loading (AC) conditions. This was done by using a complex permittivity to model the electrical behavior of the material. Because experimental results for the imaginary part of the βCN-PI/SWNT permittivity were not available, the matrix permittivity loss was varied in order to find reasonable ranges for this value. Figure 32 shows the result of varying the matrix loss of a nanocomposite with 0.1% SWNT. The real and imaginary parts of the permittivity $\varepsilon_{33}^{S}/\varepsilon_0$ are given as a function of the imaginary part of the matrix permittivity. The effective $\varepsilon'_{33}/\varepsilon_0$ shows a sharp increase as the matrix loss increases. The values of $\varepsilon'_{33}/\varepsilon_0$ before and after this jump are fairly constant. This sigmoid curve response suggests that increasing the matrix loss to a certain point could improve the dielectric properties of the composite. It is also important to note that the permittivity before the jump is exactly the same value as the static permittivity found in the static parametric study.

The S-curve plot in Fig. 32 looks very similar to results from percolation theory. It must be emphasized that percolation is not being explicitly modeled in this analysis. It is true that percolation of the nanotubes does play an important role in the actual three-phase samples. However, the FEA analysis assumes a homogenized βCN-PI/SWNT matrix with real permittivity values that correspond to experiment and imaginary permittivity values that are arbitrarily varied over a specific range. Therefore, the percolation transition that occurs in the experimental matrix as more nanotubes are added only affects the real permittivity values in this analysis. The S-curve type jump seen in the FEA results is due entirely to varying the loss component of the matrix permittivity. If the matrix loss is assumed to be proportional

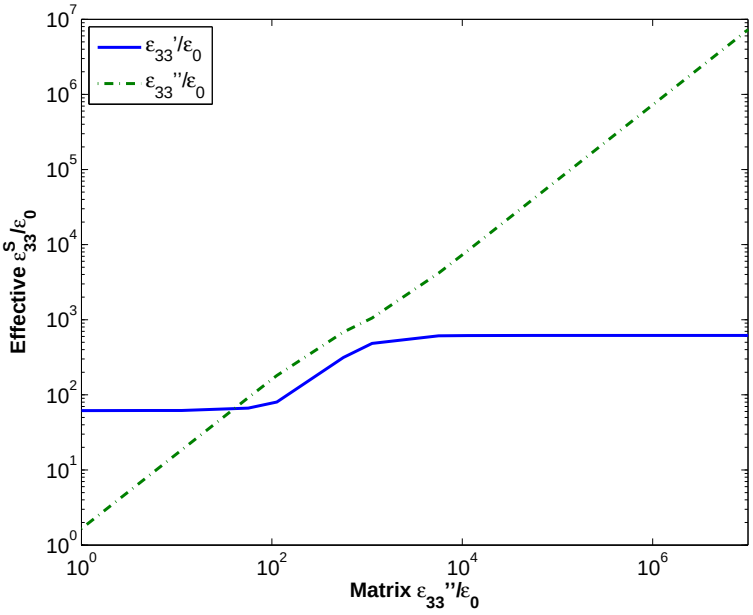

Fig. 32. Effective complex $\varepsilon_{33}^{S}/\varepsilon_0$ vs. matrix loss.

to conductivity, as in the parallel RC circuit, then the potential across the PZT is higher for greater matrix loss. This causes the electrical properties of the PZT to have a greater effect on the overall response.

The complex piezoelectric response from varying the matrix loss is given in Figs. 33 and 34 for 0.1% SWNT. Figure 33 shows the real and complex parts of e_{33} as a function of matrix loss and Fig. 34 shows a similar plot for e_{31}. Much like the complex permittivity results, the real parts of the piezoelectric coefficients show a sharp increase at approximately the same values of matrix loss. This result is extremely important because it relates directly to improving the piezoelectric response of the nanocomposite. It appears that increasing the matrix loss by adding a certain amount of nanotubes can improve the piezoelectric performance by an order of magnitude. Also, the piezoelectric coefficients before the jump are again the same values as those obtained in the static parametric study.

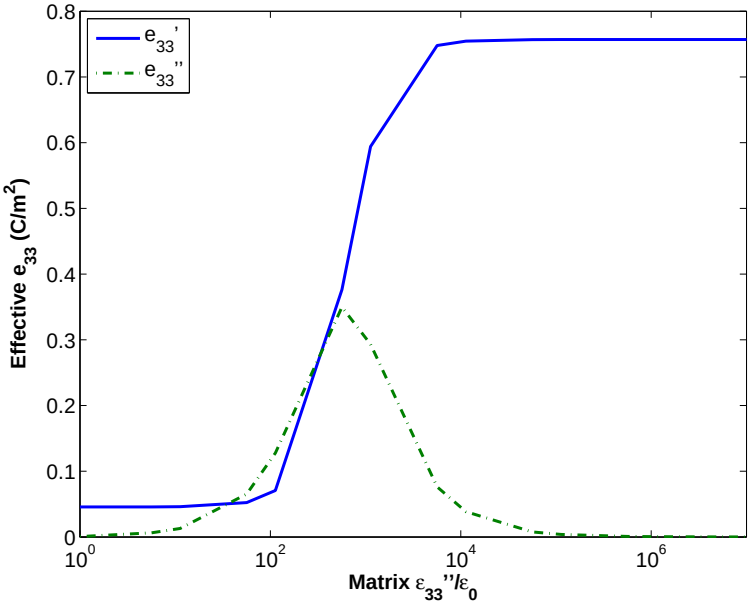

Fig. 33. Effective complex e_{33} vs. matrix loss for 0.1% SWNT.

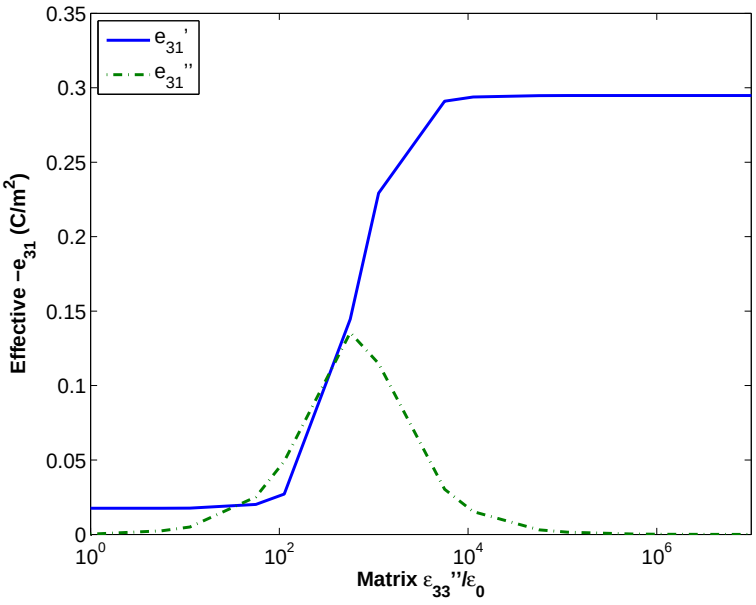

Fig. 34. Effective complex e_{31} vs. matrix loss for 0.1% SWNT.

Another way to analyze the complex piezoelectric response is to analyze the complex electromechanical coupling factors k_{33} and k_{31}. Figure 35 shows the real and imaginary parts of the complex k_{33} for 0.1% SWNT, and Fig. 36 shows k_{31} in a similar plot. The coupling factors show a sharp increase with increasing matrix loss. However, unlike the plots for $\varepsilon_{33}^{S}/\varepsilon_0$, e_{33}, and e_{31}, the coupling factors peak at a certain value of matrix loss and then decrease rapidly. This result highlights the role of the coupling factor in quantifying the efficiency of a piezoelectric material. The peak in the coupling factors shows that increasing the matrix loss will improve piezoelectric efficiency up to a point, but after that the excessive loss in the material causes the efficiency to drop rapidly.

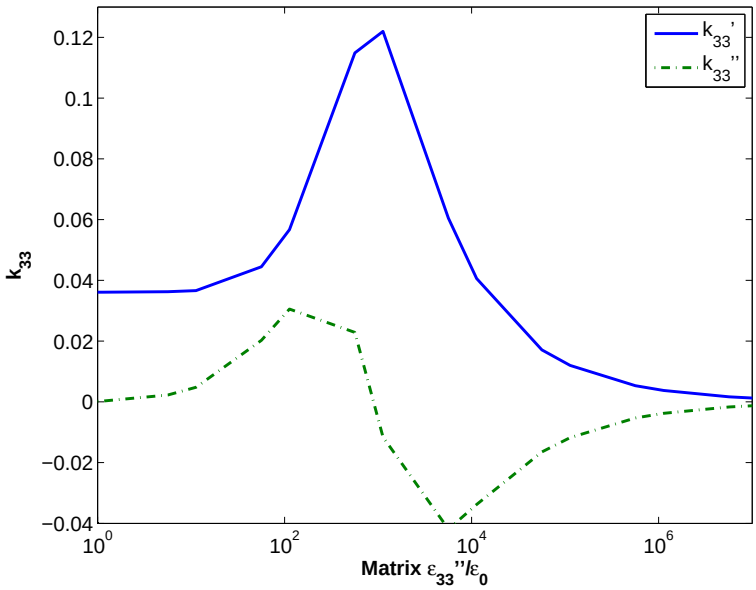

Fig. 35. Effective k_{33} vs. matrix loss for 0.1% SWNT.

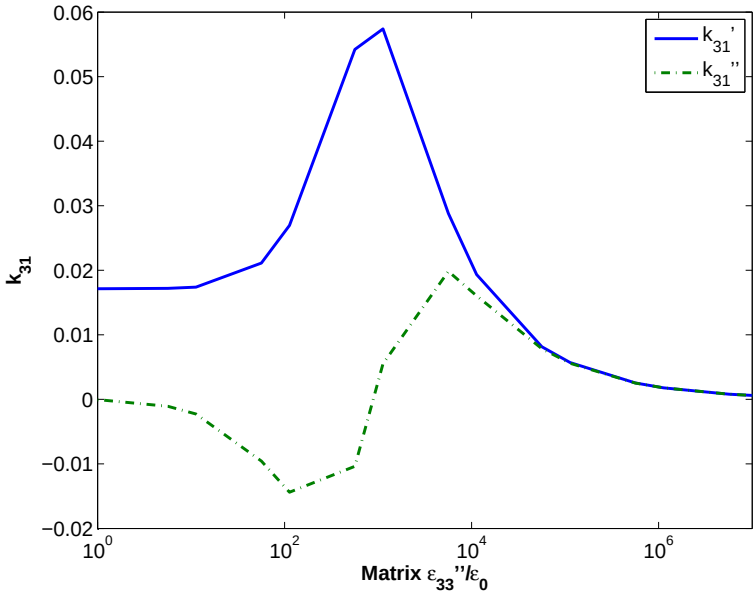

Fig. 36. Effective k_{31} vs. matrix loss for 0.1% SWNT.

D. Comparison to Other Piezoelectric Materials

The discussion of results from the static and harmonic parametric studies would not be complete without comparing predicted properties from the FEA model with properties for common piezoelectric materials that are already commercially available. This comparison is given in Table IV below. The predicted nanocomposite properties given are for a perfectly dispersed composite with matrix properties identical to the experimental values for βCN-PI/SWNT. For the harmonic loading results, the maximum real values obtained by varying the matrix loss are shown.

Table IV. Comparison of piezoelectric materials.

	PZT-5A	PVDF	βCN-PI/ 0.1% SWNT/ 20% PZT-5A	βCN-PI/ 0.2% SWNT/ 20% PZT-5A	βCN-PI/ 0.1% SWNT/ 50% PZT-5A	βCN-PI/ 0.2% SWNT/ 50% PZT-5A
e_{33}: Static	15.8	-0.027	0.04392	0.286	0.831	2.62
(C/m^2) Harmonic			0.757	0.757		
e_{31}: Static	-5.35	0.024	-0.0169	-0.11	-0.242	-0.926
(C/m^2) Harmonic			-0.295	-0.295		
k_{33}: Static	0.69		0.0355	0.0821	0.196	0.317
Harmonic			0.122	0.11		
k_{31}: Static	0.34	0.12	0.0168	0.0389	0.0804	0.137
Harmonic			0.0574	0.0518		

From Table IV it is easy to see that PZT-5A is the clear winner in terms of pure piezoelectric performance. The piezoelectric coefficients are at least an order of magnitude higher than any of the others for the materials given. However, the goal of the three-phase nanocomposite is not to have a better response than common piezoelectric ceramics. The goal is to create a composite that has a higher piezoelectric response than common piezoelectric polymers such as PVDF while exhibiting the flexibility that makes polymers useful in many applications. The table indicates that this goal is achieved, as most of the nanocomposite systems shown exhibit higher piezoelectric coefficients than PVDF. It must be noted, however, that the static coupling factor k_{31} for PVDF is higher than that for most of the nanocomposites, which indicates a more efficient conversion between the electrical and mechanical fields. Therefore, if power consumption is a concern for a particular application, the PVDF may still have an edge over some of the nanocomposite systems. Unfortunately, complex piezoelectric coefficient data for PVDF was not readily available, so the comparison must be made between the real parts of the nanocomposite results and the static PVDF values. An inspection of Table IV reveals that the real parts of the harmonic piezoelectric coefficients are at least an order of magnitude greater than the static PVDF coefficients.

Another important observation from Table IV is that under harmonic loading, there is no real benefit to using 0.2% SWNT as opposed to 0.1% SWNT. This can be seen by noticing that the real parts of the piezoelectric coefficients are the same for the two concentrations, but the coupling factors k_{33} and k_{31} are actually slightly higher for the 0.1% SWNT system. This is because of the more efficient coupling that occurs in the 0.1% SWNT material as a result of there being less dielectric loss. Therefore, if an application is strictly for AC loading, the 0.1% SWNT material would actually be the most suited.

CHAPTER V

CONCLUSIONS

A micromechanics model was developed to analyze piezoelectric composite materials. Finite element analysis was used to solve the micromechanics boundary value problem and to explore the effects of various material parameters on the effective piezoelectric properties of the composite. Scripting was used in conjunction with COMSOL Multiphysics so that all of the effective properties of a given material system could be calculated efficiently over a wide range of constituent properties.

A parametric study was performed using the LaRC-SI/PZT-7A material system. The predictions from this analysis were compared to finite element and micromechanics results from [23]. While the comparison did not completely validate the finite element model being used, it did show that the use of exact periodic boundary conditions is necessary to obtain accurate results.

A parametric study of a three-phase piezoelectric nanocomposite subject to static conditions was performed. The properties of the βCN-PI/SWNT/PZT-5A material system used were taken from [4]. The nanotube content (and thus matrix permittivity) were varied, and the predicted effective permittivities were compared to experimental results from that work. The FEA results were found to greatly over-predict the experimental properties. Therefore, several modified FEA models were created in an attempt to understand and explain this discrepancy.

The apparent permittivity of the βCN-PI/SWNT matrix used in the experimental specimens was first determined. This was done by taking the experimental properties for the three-phase specimen and numerically finding the matrix permittivity needed to obtain these exact effective properties with the FEA model. The resulting apparent permittivities of the matrix were much lower than experimental

values of the two-phase βCN-PI/SWNT specimens, and the trends with increasing nanotube content were also different. It was concluded that the original homogenized matrix properties in the FEA model were not the same as the actual properties in the three-phase specimens.

A modified model that utilized a spherical interphase region around the PZT inclusion was developed. The properties of the interphase were set to those of the neat polyimide, and the interphase volume fraction was varied to see if any resulting material distribution could replicate the experimental results of the three-phase specimens. It was found that even at the largest interphase volume fraction allowed by the geometric constraints of the problem, the effective permittivities could not match experimental values. Also, no physical basis for this material distribution could be found.

A final modified model was developed with the same interphase geometry as the polymer interphase model. This time, however, the properties of the interphase were set to the highest reasonable value of βCN-PI/SWNT permittivity obtained from experiment. The material outside of the interphase was set to properties for the neat polymer. After varying the interphase volume fraction, it was found that a material distribution that matches the effective properties to experiment could be obtained. This result indicates that if the nanotubes were agglomerated around the PZT inclusion, the effective properties of the composite would be very different from a composite with perfect dispersion. Thus, the poor dispersion of nanotubes in the three-phase composite may explain the discrepancy between FEA and experimental results. Under this assumption, it is reasonable to assume that the original effective properties predicted by FEA correspond to the response of a perfectly dispersed material. Assuming this perfect dispersion of nanotubes, the three-phase composite shows a large enhancement of piezoelectric properties (due to nanotubes) for static

loadings.

A parametric study of the original FEA model was performed for cases of harmonic loading. The real part of permittivity for the matrix was set to experimental values for βCN-PI/SWNT, and the imaginary part (matrix loss) was varied. The effective properties were all found to exhibit a sigmoid curve response when plotted against matrix loss. This indicated that there is an optimum amount of matrix loss for a given piezoelectric material system. Up to the optimum point, the matrix loss contributes to improved electromechanical performance. Past the optimum point, increasing matrix loss causes exponentially increasing effective electromechanical loss while only improving performance by a negligible amount. In this way, the βCN-PI/SWNT/PZT-5A material system can be tailored to achieve optimum performance by adding just enough nanotubes so that the matrix loss is optimal. Using this reasoning, it was found that with optimized matrix loss, there is no benefit to using 0.2% SWNT over 0.1% for harmonic loading.

The predicted properties from the static and harmonic parametric studies were compared to several common piezoelectric materials. It was seen that while the three-phase nanocomposite system studied cannot compete with traditional piezoelectric ceramics in terms of pure piezoelectric response, the system still has a response much greater than piezoelectric polymers such as PVDF. Also, the constituent makeup of the nanocomposite makes it much more flexible than a traditional ceramic. It was found that PVDF does have a higher static coupling factor k_{31} than most of the nanocomposites studied, which is an indication of a more efficient piezoelectric response. In addition, for harmonic loading, it was seen that there was no benefit to using the 0.2% SWNT material instead of the 0.1% SWNT material. This is due to the increased loss seen in the 0.2% material.

REFERENCES

[1] Liu X, Xiong C, Sun H, Dong L, Li R, Liu Y. Piezoelectric and dielectric properties of PZT/PVC and graphite doped with PZT/PVC composites. Materials Science and Engineering B 2006;127:261–266.

[2] Schlaberg H, Duffy J. Piezoelectric polymer composite arrays for ultrasonic medical imaging applications. Sensors and Actuators A 1994;44:111–117.

[3] Safari A, Lee Y, Halliyal A, Newnham R. 0-3 piezoelectric composites prepared by coprecipitated PbTiO3 powder. American Ceramic Society Bulletin 1987;66(4):668–670.

[4] Ounaies Z, Park C, Harrison J, Lillehei P. Evidence of piezoelectricity in SWNT-polyimide and SWNT-PZT-polyimide composites. Journal of Thermoplastic Composite Materials 2008;21(5):393–409.

[5] Perez R, Ounaies Z. Mechanical and electrical characterization of a 3 phase polyimide/SWNT/PZT nanocomposite and comparison with predictions of a fe model. Unpublished Raw Data 2007;.

[6] Ounaies Z, Park C, Wise K, Siochi E, Harrison J. Electrical properties of single wall carbon nanotube reinforced polyimide composites. Composites Science and Technology 2003;63:1637–1646.

[7] Potschke P, Dudkin S, Alig I. Dielectric spectroscopy on melt processed polycarbonate-multiwalled carbon nanotube composites. Polymer 2004;44:5023–5030.

[8] Potschke P, Abdel-Goad M, Alig I, Dudkin S, Lellinger D. Rheological and dielectric characterization of melt mixed polycarbonate-multiwalled carbon nanotube composites. Polymer 2004;45:8863–8870.

[9] Youngs I. Dielectric measurements and analysis for the design of conductor/insulator artificial dielectrics. IEE Proceedings - Science, Measurement, and Technology 2000;147(4):202–208.

[10] Krakovsky I, Myroshnychenko V. Modeling dielectric properties of composites by finite-element method. Journal of Applied Physics 2002;92(11):6743–6748.

[11] Sareni B, Krahenbuhl L, Beroual A, Brosseau C. Complex effective permittivity of a lossy composite material. Journal of Applied Physics 1996;80(8):4560–4565.

[12] Ang C, Yu Z, Guo R, Bhalla A. Calculation of dielectric constant and loss of two-phase composites. Journal of Applied Physics 2003;93(6):3475–3480.

[13] Zhang H, Li L, Shen Y. Modeling poling behavior of ferroelectric 3-3 composites. International Journal of Engineering Science 2005;43:1138–1156.

[14] Wu D, Chen J, Liu C. Numerical evaluation of effective dielectric properties of three-dimensional composite materials with arbitrary inclusions using a finite-difference time-domain method. Journal of Applied Physics 2007;102.

[15] White J, Poumeyrol B, Hale J, Stephenson R. Piezoelectric paint: ceramic-polymer composites for vibration sensors. Journal of Materials Science 2004;39:3105–3114.

[16] Hori M, Aoki T, Ohira Y, Yano S. New type of mechanical damping composites composed of piezoelectric ceramics, carbon black and epoxy resin. Composites: Part A 2001;32:287–290.

[17] Tian S, Wang X. Fabrication and performances of epoxy/multi-walled carbon nanotubes/piezoelectric ceramic composites as rigid piezo-damping materials. Journal of Material Science 2008;43:4979-4987.

[18] Shin B. Computation of hydrostatic piezoelectric coefficients for 1-3 composites by the finite-element method. Sensors and Actuators A: Physical 1994;40(3):191–194.

[19] Salehi-Khojin A, Jalili N. A comprehensive model for load transfer in nanotube reinforced piezoelectric polymeric composites subjected to electro-thermo-mechanical loadings. Composites: Part B 2008;39:986–998.

[20] Sherrit S, Mukherjee B. The use of complex material constants to model the dynamic response of piezoelectric materials. In: IEEE Ultrasonics Symposium. Ontario: British Crown, 1998, 1:633–640.

[21] Lamberti N, Sherrit S, Pappalardo M, Iula A. Extension to the definition of quasistatic material coupling factor to include losses. IEEE Transactions on Ultrasonics, Ferroelectrics, and Frequency Control 2005;52(6):1026–1034.

[22] Piquette J, McLaughlin E. Full solution, for the crystal class 3m, of the Holland-EerNisse complex material-constant theory of lossy piezoelectrics for harmonic time dependence. IEEE Transactions on Ultrasonics, Ferroelectrics, and Frequency Control 2007;54(6):1250–1264.

[23] Odegard G. Constitutive modeling of piezoelectric polymer composites. Acta Materialia 2004;52:5315–5330.

[24] Silva E, Fonseca J, Kikuchi N. Optimal design of periodic piezocomposites. Computer Methods in Applied Mechanics and Engineering 1998;159:49–77.

[25] Berger H, Kari S, Gabbert U, Rodriguez-Ramos R, Guinovart R, Otero J et al. An analytical and numerical approach for calculating effective material coefficients of piezoelectric fiber composites. International Journal of Solids and Structures 2005;42:5692–5714.

[26] Kelly J, Ballato A, Safari A. The effect of complex piezoelectric coupling coefficient on the resonance and antiresonance frequencies of piezoelectric ceramics. In: Proc. of the Tenth IEEE International Symposium on Applications of Ferroelectrics. IEEE, 1996, 2:825-828.

[27] COMSOL Multiphysics User's Guide. Stockholm, Sweden: COMSOL AB; 2007.

[28] Leo D. Engineering analysis of smart material systems. Hoboken, NJ: John Wiley & Sons; 2007.

[29] Kasap S. Principles of electronic materials and devices. New York: McGraw-Hill; 2002.

[30] Cavicchi T. Fundamentals of electrical engineering: Principles and applications. Englewood Cliffs, NJ: Prentice-Hall; 1993.

[31] Rizzoni G. Principles and applications of electrical engineering. New York: McGraw-Hill; 2004.

[32] Hippel A. Dielectrics. In: Condon E, Odishah H, editors. Handbook of physics. New York: McGraw Hill; 1967. p. 4-102–4-128.

[33] Kremer F, Schonhals A. Broadband dielectric spectroscopy. Berlin: Springer-Verlag; 2003.

[34] Piquette J, McLaughlin E. The use of real or complex coupling coefficients for lossy piezoelectric materials. IEEE Transactions on Ultrasonics, Ferroelectrics, and Frequency Control 2009;56(4):821–826.

[35] Whitcomb J, Chapman C, Tang X. Derivation of boundary conditions for micromechanics analyses of plain and satin weave composites. Journal of Composite Materials 2000;34(9):724–747.

[36] Poon Y, Ho C, Wong Y, Shin F. Theoretical predictions on the effective piezoelectric coefficients of 0-3 PZT/polymer composites. Journal of Material Science 2007;42:6011–6017.

[37] Chan H, Chen Y, Choy C. A poling study of PZT/P(VDF-TrFE) copolymer 0-3 composites. Integrated Ferroelectrics 1995;9:207–214.

[38] Furukawa T. Piezoelectricity and pyroelectricity in polymers. IEEE Transactions on Electrical Insulation 1989;24(3):375–394.

[39] Venkatragavaraj E, Satish B, Vinod P, Vijaya M. Piezoelectric properties of ferroelectric PZT-polymer composites. Journal of Physics D: Applied Physics 2001;34:487–492.

[40] Paradies R, Schlapfer B. Finite element modeling of piezoelectric elements with complex electrode configuration. Smart Materials and Structures 2009;18:1–13.

[41] Sandler J, Shaffer M, Prasse T, Bauhofer W, Schulte K, Windle A. Development of a dispersion process for carbon nanotubes in an epoxy matrix and the resulting electrical properties. Polymer 1999;40:5967–5971.

VITA

Name:	Kevin S. Maxwell
Address:	Texas A&M University
	Department of Aerospace Engineering
	H.R. Bright Building, Rm. 701, Ross Street - TAMU 3141
	College Station TX 77843-3141
Email Address:	kmax@tamu.edu
Education:	B.A., Aerospace Engineering, Texas A&M University, 2007
	M.S., Aerospace Engineering, Texas A&M University, 2009